

UNIVERSITY OF OKLAHOMA  
GRADUATE COLLEGE

HIGHLY MINIATURIZED VHF HELICAL FILTERS WITH FULLY  
RECONFIGURABLE CAPABILITIES

A THESIS  
SUBMITTED TO THE GRADUATE FACULTY  
in partial fulfillment of the requirements for the  
Degree of  
MASTER OF SCIENCE

By  
EIVY ARROYO DIAZ  
Norman, Oklahoma  
2019

HIGHLY MINIATURIZED VHF HELICAL FILTERS WITH FULLY  
RECONFIGURABLE CAPABILITIES

A THESIS APPROVED FOR THE  
SCHOOL OF ELECTRICAL AND COMPUTER ENGINEERING

BY

Dr. Hjalti Sigmarsson, Chair

Dr. Shahrokh Saeedi, Co-Chair

Dr. Jay McDaniel

© Copyright by EIVY ARROYO DIAZ 2019  
All Rights Reserved.

*This thesis is dedicated to our gracious and compassionate God “in whom are hidden all the treasures of wisdom and knowledge,” to my son Ethan who completely changed my life and inspired me to become something bigger than myself, and to my wonderful, intelligent, and selfless wife Blandy who supported me through every step of this amazing journey.*

## Acknowledgments

There are many I wish to thank that provided advice and who have helped me work toward this thesis, beginning with my committee members. Dr. McDaniel has a special way of explaining complex theoretical concepts in very simplified and understandable manner. He was my professor for an advanced electromagnetics course and I truly enjoyed how simple he made everything seem. His successful career and accomplishments have been an inspiration to me and I'm very thankful to have had his advice and guidance throughout this experience. I would also like to sincerely thank Dr. Saeedi who offered an abundance amount of advice, guidance, and encouragement during my studies. His understanding of this work has been extremely valuable to me and the development of this work. From theoretical concepts to fabrication suggestions, his experience and willingness to help have guided me through many difficult stages of this work. He is an extraordinary teacher, mentor, and friend who I could not appreciate more. Finally, I would like to thank Dr. Sigmarsson for believing in my potential. Before he was my official advisor, he had been providing academic and career advice as far back to my undergraduate studies. His genuine interest in students was shown by his willingness to help and provide motivation to meet my goals. The depth of insight he provided was truly an inspiration. I was always surprised of how fast he was able to resolve an issue that I had been stuck on for hours, in a matter of minutes. He would

test my understanding on the subject matter by asking tough questions, only to make me more confident when attending competitive conferences. This confidence has transferred over to my future career as I begin a new chapter in the industry. I cannot be more grateful to have worked alongside them all and hope that one day I am as knowledgeable and resourceful to others.

I am also very grateful of my in-laws, Jose and Consuelo for believing in me and providing an incredible amount of help during my academic career. I could not have done this without their support. Mama, el hombre que soy hoy es debido a un ejemplo de una fuerte mujer como usted. Gracias por todos sus consejos y oraciones. Mario, Miguel, and Perla thank you all for your encouragement, patients, and amazing support throughout the past years. Thank you to all my friends and fellow members at the RIL, especially for all the extremely helpful advice and guidance through HFSS and fabrication. I wish you all nothing but the best.

# Table of Contents

<b>Acknowledgments</b>	<b>vi</b>
<b>Abstract</b>	<b>xiv</b>
<b>1 Introduction</b>	<b>1</b>
1.1 Overview . . . . .	1
1.2 Microwave Filters from Past to Current . . . . .	2
1.2.1 Lumped Elements . . . . .	3
1.2.2 Helical Resonator Filter Technology . . . . .	5
1.3 Motivation . . . . .	11
1.4 Outline of the Thesis . . . . .	12
<b>2 Highly Miniaturized Helical Resonators</b>	<b>14</b>
2.1 Introduction . . . . .	14
2.2 Design Guidelines . . . . .	14
2.3 Previous Work Validation . . . . .	17
2.3.1 Simulation . . . . .	20
2.3.2 Fabrication and RF Measurements . . . . .	21
2.4 Proposed Design . . . . .	26
2.5 Discussion on Capabilities & Improvements . . . . .	30
2.6 Conclusion . . . . .	31

<b>3</b>	<b>Tunable Second Order Helical Filters</b>	<b>32</b>
3.1	Introduction . . . . .	32
3.2	Helical Resonator Filter Design . . . . .	33
3.3	Experimental Validation . . . . .	37
3.4	Discussion on Capabilities & Improvements . . . . .	43
3.5	Conclusion . . . . .	44
<b>4</b>	<b>Fully Reconfigurable Filters</b>	<b>45</b>
4.1	Introduction . . . . .	45
4.2	Design and Simulation . . . . .	46
4.3	Experimental Validation . . . . .	50
4.4	Discussion on Capabilities & Improvements . . . . .	57
4.5	Conclusion . . . . .	58
<b>5</b>	<b>Fully 3D-Printed Helical Resonators</b>	<b>59</b>
5.1	Introduction . . . . .	59
5.2	Design . . . . .	60
5.2.1	Fabrication & Experimental Validation . . . . .	62
5.3	Discussion on Capabilities & Improvements . . . . .	67
5.4	Conclusion . . . . .	68
<b>6</b>	<b>Conclusion</b>	<b>69</b>
6.1	Future Direction . . . . .	70
	<b>References</b>	<b>72</b>



## List of Tables

1.1	Summary of Resonator and Filters Presented in this Thesis . .	13
2.1	Highly Miniaturized Helical Resonator Design Parameters . .	19
3.1	Second-Order Filter Design Parameters . . . . .	35
4.1	Fully Reconfigurable Miniaturized Filter Design Parameters .	48
5.1	3D-Printed Helical Resonator Design Parameters . . . . .	62
5.2	$Q_{un}$ Comparison of the 3D-Printed and Wire-Formed Helix . .	68

## List of Figures

1.1	Frequency allocations and regulations in the U. S. with the area of interest circled (adapted from [2]). . . . .	2
1.2	Side internal view of a traditional helical resonator filter design with extra emphasis on the apertures, tuning screws, and tap lines (from [19]). . . . .	6
1.3	(a) Conceptual model of a miniaturized tunable helical resonator and (b) a visual electric field representation of the capacitively loaded helical resonator inside an air-filled shielded cavity (from [20]). . . . .	7
1.4	(a) Frequency response of a fabricated tunable helical resonator for various states and (b) a $Q$ comparison between measurement and simulation (from [20]). . . . .	8
1.5	(a) Conceptual model of a helical resonator filter with an inline interdigital coupling configuration and (b) frequency response (from [16]). . . . .	9
1.6	Photograph of a 3D-printed then silver plated helical resonator filter (from [21]). . . . .	10
2.1	Helical resonator with a circular cross section defining parameters (from [26]). . . . .	15

2.2	Internal view of the highly miniaturized tunable helical resonator with variable capacitive loading. . . . .	18
2.3	Conceptual model of the highly miniaturized tunable helical resonator with all components labeled. . . . .	19
2.4	(a) Quality factor versus capacitive gap size and (b) resonant frequency versus capacitive gap size. . . . .	21
2.5	(a) Overview of the fabrication process and (b) exploded view of the highly miniaturized helical resonator. . . . .	22
2.6	Photograph of the 3D-printed coil former . . . . .	23
2.7	Comparison of the simulated and measured results of the cavity without the helix. . . . .	24
2.8	Measured results of (a) electrically tuning the resonant frequency and (b) mechanically tuning the resonant frequency . . . . .	25
2.9	Conceptual model of the proposed miniaturized tunable helical resonator including an equivalent circuit of the resonator. . . . .	27
2.10	Internal view of the conceptual model of the proposed miniaturized tunable helical resonator. $D = 28$ mm, $d = 14.4$ mm, $h = 14$ mm, $\alpha = 1.6$ mm, $p = 2.2$ mm, and the number of turns $N = 3.4$ . . . . .	28
2.11	Measured response of the fabricated highly miniaturized tunable helical resonator at various states, (a) Transmission versus frequency response. (b) Extracted unloaded $Q$ from measured S-parameters. . . . .	29
2.12	Photograph of the fabricated miniaturized tunable helical resonator with the cover off (left) and fully assembled (right). . . . .	30

3.1	Calculated relationship between (a) $K_{1,2}$ and $D_{res}$ and (b) $Q_{ext}$ and $\phi$ . . . . .	34
3.2	Model of the miniaturized tunable helical resonator filter. (a) Showing dimensions of the different parts of the filter assembly. (b) Defining the reference point for the L-bar tap point. (c) Showing the location where the L-bar taps to the helix. . . . .	36
3.3	Photograph of the fabricated prototype of the second-order tunable helical resonator filter. . . . .	37
3.4	Measured frequency responses of the fabricated tunable helical resonator filter at various capacitance states. (a) Transmission response versus frequency. (b) Input reflection response versus frequency. . . . .	38
3.5	(a) Zoomed in plot of the transmission response versus frequency. (b) Relationship between the insertion loss as a function of frequency. . . . .	39
3.6	Proposed coupling diagram of the tunable helical filter. . . . .	40
3.7	(a) AWR schematic implementing additional paths of energy transfer causing two transmission zeros and a (b) frequency response of the AWR schematic and HFSS results overlayed at a sample of 200 MHz. . . . .	41
3.8	(a) Comparison of simulated and measured S-parameter responses at 200 MHz. (b) Comparing second-order bandpass filter responses utilizing Butterworth, Chebyshev, and simulated results of the proposed prototype helical filter at 200 MHz. . . . .	42
4.1	Conceptual model of the fully reconfigurable miniaturized helical resonator filter with labeled varactor diodes. . . . .	46

4.2	Conceptual design model of proposed reconfigurable helical filter (a) top view highlighting the roll of each group of varactors and (b) equivalent circuit representation. . . . .	47
4.3	Internal view of the proposed helical filter defining new parameters. . . . .	48
4.4	(a) Simulated frequency response of the fully reconfigurable helical filter showing an example of having constant absolute bandwidth of 8 MHz throughout the sweep. (b) Simulated relationship between the insertion loss and bandwidth with respect to the frequency sweep. . . . .	49
4.5	Photographs of the fabricated fully reconfigurable filter. . . . .	50
4.6	Photograph of the setup prior to obtaining measurements showing (a) all the power supplies that were required for tuning and a (b) zoomed in photograph of the filter. . . . .	51
4.7	Measured behavior of insertion loss and bandwidth versus frequency demonstrating constant absolute bandwidth of 8 MHz. . . . .	52
4.8	Measured results of the proposed fabricated reconfigurable filter demonstrated with 8 MHz absolute bandwidth across the whole tuning range with the (a) transmission versus frequency and (b) input reflection versus frequency. . . . .	53
4.9	Measured results of the same fabricated reconfigurable filter with various sample of 10 MHz absolute bandwidth (a) transmission versus frequency and (b) input reflection versus frequency. . . . .	54
4.10	Measured results of the same fabricated reconfigurable filter demonstrating constant fraction bandwidth with (a) transmission versus frequency and (b) input reflection versus frequency. . . . .	55

4.11	Measured behavior of insertion loss and bandwidth versus frequency from the results demonstrating constant absolute bandwidth of 10 MHz. . . . .	56
4.12	Measured behavior of insertion loss and bandwidth versus frequency from the results demonstrating constant fractional bandwidth. . . . .	56
5.1	Exploded model of a highly miniaturized 3D-printed tunable helical resonator with varactor diodes mounted on the PCB. .	61
5.2	Internal view of the proposed 3D-printed helical resonator with defined parameters. . . . .	62
5.3	Illustration of the fabrication process. Starting from 3D-printing, then to copper plating, assembling the parts, and the final product. . . . .	63
5.4	(a) Photograph of the 3D-printed helix with printed supports and a (b) photograph after the removal of supports. . . . .	64
5.5	Photographs of the fabricated fully 3D-printed helical resonator. Cover removed to show helix (left) and fully assembled (right).	65
5.6	Measured frequency response of the fully 3D-printed resonator.	66
5.7	Measured unloaded $Q$ from the 3D-printed helical resonator. .	67

## Abstract

The demand for frequency reconfigurable bandpass and bandstop filters within the VHF-UHF frequencies continues to rise due to the increasingly crowded radio frequency (RF) spectrum. As a result, higher levels of isolation and an increase in selectivity are essential for the next-generation of intelligent microwave communication systems. Additionally, compact structures that maintain performance and are integratable with other RF components are very desirable. One way to cope with this reality is to investigate reconfigurable capabilities while reducing the physical size of well-known high-performance structures in the VHF-UHF realm. This thesis presents a second-order bandpass filter to demonstrate a method of miniaturizing a helical resonator filter utilizing varactor diodes as the capacitive loading element. This technique not only miniaturizes the helical structure but also allows for a voltage-controlled resonant frequency tuning mechanism. To achieve agility in the external coupling as well as the inter-resonator coupling, a new method of coupling into the helical structures is used to incorporate the use of varactor diodes as a tuning element. As a result, a fully reconfigurable miniaturized helical bandpass filter is simulated, fabricated, and measured, offering promising results for dynamic frequency access in future wireless systems.

# Chapter 1

## Introduction

### 1.1 Overview

Currently, technology advancements have led to an exponential rise of accessible wireless devices. As a result, the challenge of dealing with an ever-crowded frequency spectrum becomes more difficult year after year. It can be shown from Fig. 1.1 that the upper portion of the radio spectrum is severely overcrowded. This challenge gives rise to the demand for sophisticated microwave systems with agile front-ends that enable cognitive frequency response control with dynamic capabilities in the very high frequency (VHF) and ultra high frequency (UHF) frequency bands. The VHF band has a range of frequencies that are of 30-300 MHz and the UHF band has the range of 300-3000 MHz, which can be seen in Fig. 1.1. Additionally, television (TV) white space spectrum in the VHF-UHF bands has recently been released by the Federal Communication Commission (FCC) and is expected to foster novel long-range wireless applications, in which the use of advanced-hardware integrated frequency-agile software-based radios is desirable [1]. White space is a term used by the FCC for unused TV spectrum and access to this new spectrum comes with technical challenges. In the sub-gigahertz frequency vicinity, where the wavelength is



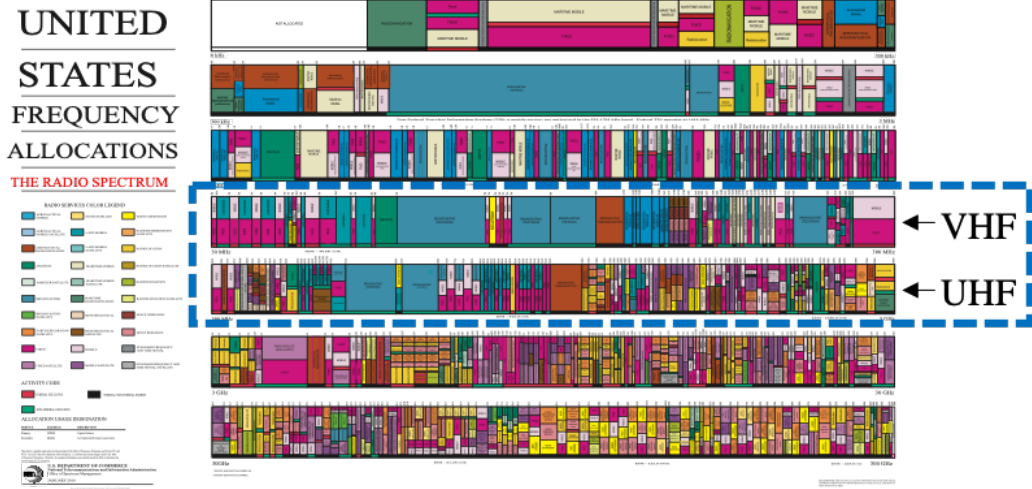


Figure 1.1: Frequency allocations and regulations in the U. S. with the area of interest circled (adapted from [2]).

on the order of several feet (e.g., approximately 5 ft. at 200 MHz), realizing compact reconfigurable filters while maintaining a high unloaded quality factor ( $Q$ ) remains a challenge.

## 1.2 Microwave Filters from Past to Current

An electronic filter is simply an electric circuit that experiences frequency-dependent characteristics. Essentially, filters are devices that are used to accept and pass desirable frequencies while rejecting unwanted frequencies. Unwanted frequencies can come from the interaction between various radio frequency (RF) components in a system as well as undesired spurious signals coming from the input signal. Filters enable a system to select or confine the signals of interest by utilizing energy-storage elements. As the unloaded  $Q$  is a ratio of stored energy versus dissipated energy, selecting high- $Q$  technology/technologies for the filter design, set the foundation for this work. Common filter technologies that implement different types of energy-storage ele-

ments are described as follows. Discrete inductor-capacitor (LC) resonators are the simplest circuit that can be used for a filter design. The circuit consist of series or parallel inductors and/or capacitors. Technologies that include microstrip lines, coplanar waveguides, and striplines all are categorized under planar transmission lines. These technologies utilize metal traces to achieve resonators and filters while having the advantage of being on a planar platform [3]. Another common technology for filter design include coaxial resonators, measuring a quarter-wavelength of the resonant frequency. A coaxial resonator consists of a conductive transmission line within a shield. The inner conductor is solidly connected to the shield on one end while the other end is open-circuited. There are also cavity resonators, which is made up of a hollow conductive box or cavity that has the capability of storing electromagnetic energy [4]. As a result, devices featuring high  $Q$ s and low insertion loss can be realized. In the following section, these different technologies are investigated to highlight key features that are used to determine the design of this work.

### **1.2.1 Lumped Elements**

A common method of realizing filters operating in the VHF-UHF realm is by applying the concept of integrating lumped elements with planar-based transmission lines, such as microstrip line coplanar waveguide, or coplanar stripline. Lumped elements are utilized to achieve tuning capabilities and some of the common technologies that are available in open literature include CMOS varactors [5], ferroelectric metal-insulator-metal (MIM) capacitors [6]–[8], and RF- microelectromechanical systems (MEMS) [9]–[11]. These types of devices provide desirable features such as low profile, rapid tuning speeds, and a relatively wide tuning range. However, due to the general limitations

associated with lumped elements, their applicability is limited by high insertion loss as the quality factor is in the range of approximately 20-50 and low RF power handling that ranges from 20-30 dBm. The different tuning technologies mentioned here are summarized as follows.

The authors of [12] present a second-order LC bandpass filter that reports a tuning range of 11% at an operating frequency of 1 GHz and a  $Q$  that ranges from 5-180. The following filters use the concept of employing static inductors and tunable surface mount varactors in order to achieve frequency tunability. Varactor diodes are typically utilized in the filter resonant circuitry. By applying a reverse voltage to the varactors, a variable capacitance can be obtained. Furthermore, by having control over the reverse bias, a tunable resonant frequency of the circuit can be achieved. The tuning range of the filter is determined by the maximum bias and minimum bias applied to the varactors. For example, a second-order bandpass filter using tunable varactors and multilayer organic substrate are introduced in [5]. In this publication, the frequency achieves a tuning range of 510-910 MHz and an insertion loss that ranges from 1.83-2.45 dB, which has a corresponding  $Q$  less than 34. Additionally, a low-temperature co-fired ceramic (LTCC) integrated fourth-order tunable filter with a tunable frequency range of 100-200 MHz, an insertion loss below 2.15 dB, and a  $Q$  less than 35 was demonstrated in [13]. Although the varactors are used to demonstrate and achieve an impressive tuning range, while maintaining a low profile, alternatives need to be investigated to achieve higher power handling capabilities.

Ferroelectric varactors are used to improve the  $Q$  in [6] and [7]. First, a second-order bandpass filter reported a tunable frequency range of 385-420 MHz and a  $Q$  that has a range of 45-72 in [6]. Similarly, a second-order

bandpass filter shows to have a tuning range of 300-450 MHz and a  $Q$  that ranges from 71-85. Both of these filters use low dielectric loss materials and shows improvement in  $Q$ ; however, the tuning range is sacrificed.

Additionally, methods to improve linearity and power handling are also presented in [9]–[11]. One method shown by the authors in [10] is the use of RF-MEMS to achieve a bandpass filter [9] operating in VHF band with power handling of 40 dBm at the expense of a  $Q$  of 10. A second-order bandpass filter operating at comparable frequencies is shown to have an improvement in the  $Q$  that ranges from 52-73, while having relatively high linearity performance (IIP<sub>3</sub>) greater than 68 dBm.

### **1.2.2 Helical Resonator Filter Technology**

In the following section, tunable filters that utilize waveguide resonators as the fundamental component are considered as an alternative method to overcome the low  $Q$  and power handling associated with lumped elements. In [14], the concept of utilizing high  $Q$  dielectric materials to realize dielectric resonator filters with  $Q$  values of 4000 and above is presented. However, for some applications, this method might come with sacrificing the desirable low profile.

The use of helical resonator filter technology in radio frequency applications has been well known as early as the mid 1950's. A helical resonator is made up of a shield with an inner conductor formed into a helix and typically have a circular cross section. A helical resonator resembles a coaxial resonator as the two main components include an inner conductor inside a shield [15], [16]. Similar to the coaxial resonator, the length of the coil is a quarter-wavelength of the resonant frequency. Additionally, one end of the coil is solidly con-

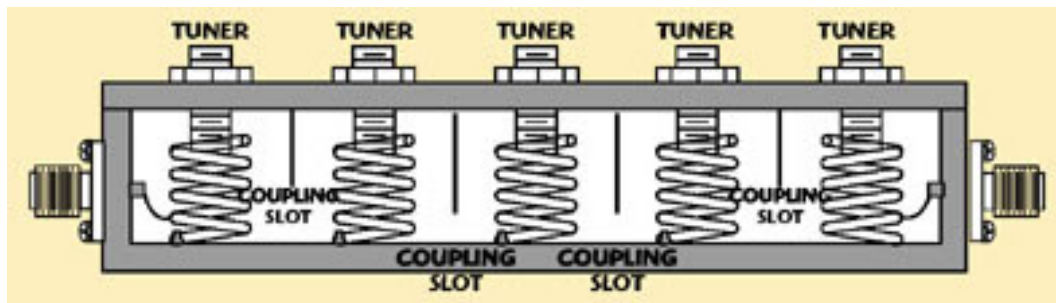


Figure 1.2: Side internal view of a traditional helical resonator filter design with extra emphasis on the apertures, tuning screws, and tap lines (from [19]).

nected to the shield while the other end is open-ended. A helical resonator employs many of the high performance features as the coaxial resonator, such as a high unloaded  $Q$  and high power-handling, while maintaining a compact size [17], [18]. Helical resonators become extremely useful when the electrical performance of traditional lumped-element components deteriorate at higher frequencies [4]. Furthermore, the extensive use of satellites and ground-based mobile communication systems in the VHF-UHF bands presents a robust physical limitation. At the lower end of the VHF band, a TEM-mode coaxial-line resonator maintains a high  $Q$ , but becomes impractical as the physical size is approximately 8 feet in length. For this reason, helical resonators are best suited for applications where low-profile and superior electrical performance are essential.

A helical resonator filter, in its most conventional form, consist of several helical resonators inside a shielded cavity that can be of either circular or square cross section. The helical resonators are coupled to each other through an inline or staggered configuration by having openings, which are called apertures, in the cavity walls that separate them, as shown in Fig. 1.2. The helical resonators are essentially quarter-wave sections of a shielded transmission line formed into a helical structure. Fig. 1.3a shows a resonator is grounded (short-

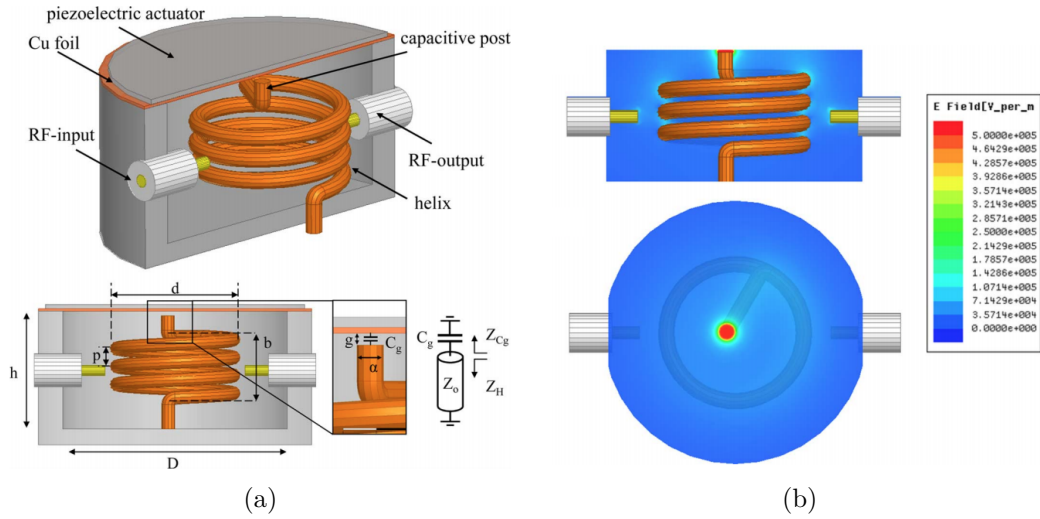


Figure 1.3: (a) Conceptual model of a miniaturized tunable helical resonator and (b) a visual electric field representation of the capacitively loaded helical resonator inside an air-filled shielded cavity (from [20]).

circuited to the cavity) at one end and open-circuited at the other end.

The input and output coupling of a helical resonator filter is accomplished by tapping directly to the helix at a low electric field point, which essentially provides impedance matching to the source and load. Screws are utilized as tuning mechanisms by placing them above the helical resonator where the open-circuited end is located and where there is a high concentration of electric field as demonstrated in Fig. 1.3b. Finally, the bandwidth of the helical filter is controlled by the aperture size and location.

Traditionally, helical resonator filters have been designed to operate at fixed frequencies. Moreover, they are typically connectorized to facilitate integration with the rest of the RF system. As a result, the increase of the physical size and weight brings a significant disadvantage to a modern integrated system design. On the other hand, modern communication systems require higher levels of hardware integration and frequency-agility for implementing cognitive

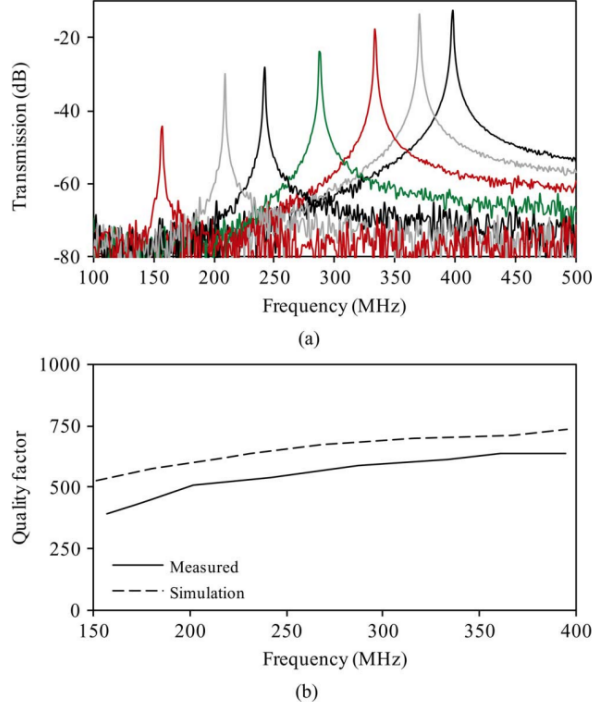


Figure 1.4: (a) Frequency response of a fabricated tunable helical resonator for various states and (b) a  $Q$  comparison between measurement and simulation (from [20]).

and software-defined radios. Recently, a method demonstrating how to miniaturize helical resonators utilizing capacitive loading was introduced in [20] and a conceptual model of this helical resonator design is shown in Fig. 1.3a. In this publication, a capacitive gap is used to apply heavy capacitive loading to the cavity. This method suggests that by countering the inductive loading that is required to resonate at a specified frequency with capacitive loading, a smaller helical resonator can be realized, therefore miniaturizing the entire device. Furthermore, the lattice structure of the piezoelectric actuator disk can be controlled by tuning the bias voltage applied to the piezoelectric actuators. The disk then flexes up or down changing the capacitive gap between the top cavity cover and the open-circuited end of the helix, thereby tuning the

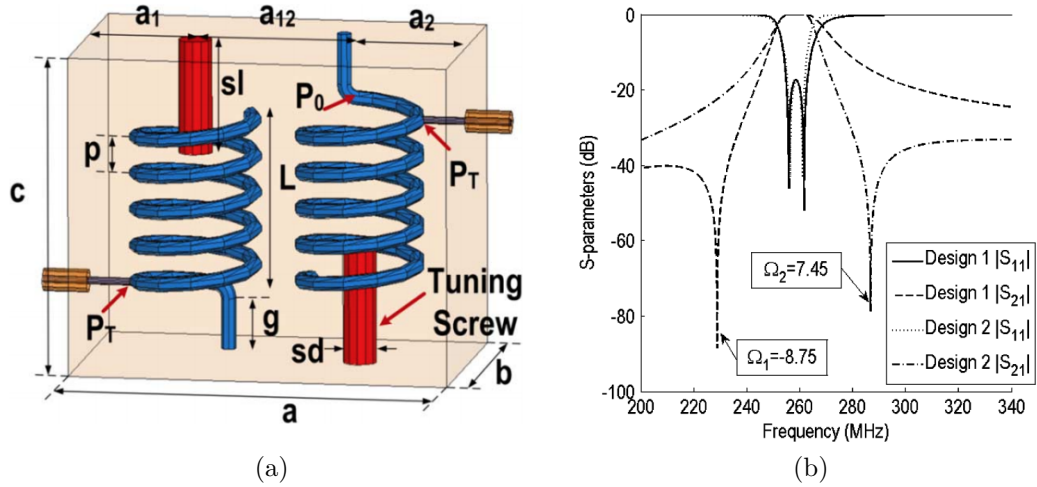


Figure 1.5: (a) Conceptual model of a helical resonator filter with an inline interdigital coupling configuration and (b) frequency response (from [16]).

resonant frequency. A plot demonstrating the tunable range of 257-365 MHz is shown in Fig. 1.4. It can also be seen that this particular resonator achieved an unloaded  $Q$  that ranges from 392-639 in Fig. 1.4. The measured insertion loss associated with the tuning range is 0.3-3.2 dB. The bandwidth is 6%–7% with a compact internal volume of 8.6 cm<sup>3</sup>.

Additional features, such as incorporating a transmission zero (TZ) in the response of a second-order inline helical resonator filter, has been introduced in [16]. In this publication, an inline interdigital coupling topology, as seen in Fig. 1.5a, is used to achieve a pseudo-elliptic response and allows the helical resonator filter the ability to select the position of a transmission zero (TZ) in the stopband. Fig. 1.5b demonstrates two iterations of the frequency response, each iteration with the TZ positioned on the opposite side of the stopband. This study reported a helical filter operating at 244 MHz with dimensions of the order of  $0.05\lambda$ , power handling capability up to 90 W, 8 MHz bandwidth,



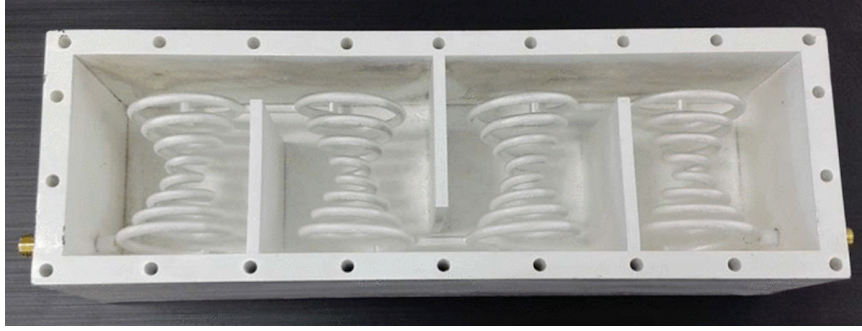


Figure 1.6: Photograph of a 3D-printed then silver plated helical resonator filter (from [21]).

unloaded  $Q$  of 1224, and a measured insertion loss of 0.18 dB, furthermore, the filter had including an improved skirt selectivity from the transmission zero.

A traditional method of realizing a helical resonator typically involves robust manufacturing such as computer numeric control (CNC) machining to carve out a block of copper and helix molds, which can not only be expensive but also time consuming. Furthermore, for an accurate fabrication and in order to compensate for inaccuracies introduced during the manufacturing process, tuning screws are used to optimize the performance of the helical resonator filter. Additionally, soldering the joint between the helix and the inner walls of the shielded cavity is typically performed to ensure a solid electrical connection. This portion of the fabrication is especially important as it plays a major roll in the quality factor of the device. However, the current trend of 3D-printing various prototype structures is becoming an increasingly attractive alternative method of fabrication as manufactures are producing 3D-printers with impressively high resolution. 3D-printing technologies open the door to an inexpensive method of rapidly prototyping RF structures. Some examples of microwave component that were 3D-printed and that have been published can be found in [22]–[24]. More specifically, a method of 3D printing

a fourth-order helical resonator bandpass filter is shown in [21]. The helix and cavity are first 3D printed together as a standalone piece and the 3D-printed structure is put through a metallization process, as seen in Fig. 1.6. This eliminates the inaccuracies presented while soldering the joint between the helix and cavity as the entire structure is coated with metal. In this publication, the helical filter is designed to operate at 500 MHz with 4% fractional bandwidth.

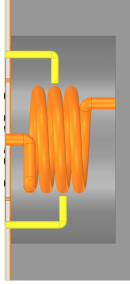
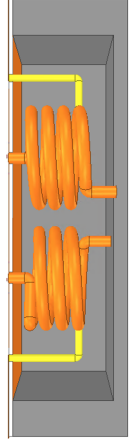
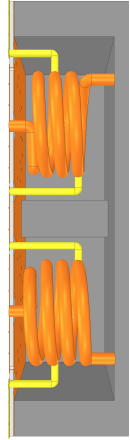
### 1.3 Motivation

The motivation for this work is to provide devices in the VHF-UHF range that incorporates multiple features that are desirable in future filters. These features include compact size, continuous tuning capabilities, reconfigurable capabilities, rapid tuning speeds, high  $Q$ , low insertion loss, and being integratable with the rest of the RF system. A helical resonator is a great candidate to investigate as it provides some key features such as high  $Q$  and compact size. Furthermore, to the best of the author's knowledge, there are only two publications reporting helical resonators with tuning capabilities in [20], [25]. The authors in [25] demonstrated a second-order helical filter that achieved tunability by using p-i-n switching capacitors. In this publication, a low insertion of 0.8-1.2 dB and a wide tuning range was reported; however, its functionality is limited to five tuning states and occupies a relatively large internal volume of 216 cm<sup>3</sup>. In [20], a highly miniaturized helical filter is presented with continuous tuning capabilities; however, the bandwidth is not maintained constant throughout the tunable range. Therefore, the motivation of this work is to integrate helical resonators with semiconductor technology with the concept of yielding high- $Q$  compact structures with rapid-tuning surface-mount components.

## 1.4 Outline of the Thesis

The purpose of this thesis is to present a fully reconfigurable filter for VHF applications that not only features highly compact size but also allows for integration of future RF components directly on the proposed device. A helical resonator is chosen as the fundamental component of the device that will provide some of the key features that are desirable in a filter. Therefore, Chapter 2 includes the guidelines to acquire dimensions for a single resonator based on design specifications. Additionally, a full characterization of the helical resonator is performed as it serves as a building block for higher order filters. Chapter 3 goes into details of a 4% tunable second-order Butterworth band-pass filter that was designed, simulated, fabricated, and tested for validation. Chapter 4 presents the fully reconfigurable helical resonator filter. With simulation and measured results, it is shown that a user is in full control of having either constant absolute bandwidth (ABW), constant fractional bandwidth (FBW), or constant insertion loss (IL) across the full range of the tunable frequency sweep. Chapter 5 goes into the details of the fabrication process that was used throughout this work. Specifically, the 3D-printing technologies are put to the test with a design of a fully 3D-printed helical resonator. Table 1.1 shows the progression of the this study while highlighting some of the important features that were achieved at each stage. Finally, Chapter 6 concludes with a summary and discussion on the future direction of the work presented.

Table 1.1:  
Summary of Resonator and Filters Presented in this Thesis

Property	Chapter 2:	Chapter 3:	Chapter 4:
	Resonator	Tunable	Reconfigurable
Device Type	Characterization 	Helical Filter 	Helical Filter 
Features	$f_o$ : 150-220 MHz $Q$ : 185-234	$f_c$ : 170-230 MHz IL: 0.9-1.3 dB	Constant ABW Constant FBW
	Novel Tap Lines	2 TZs	Constant IL

## Chapter 2

### Highly Miniaturized Helical Resonators

#### 2.1 Introduction

In order to move forward with designing multiple order filters, a first order resonator of the chosen structure that must first be designed and characterized. This provides insight on the electrical performances such as the unloaded  $Q$  and tuning range of the structure. The  $Q$  is used as a figure of merit as it is a measure of stored energy versus dissipated energy. In this Chapter, a step-by-step process to obtain dimensions of a helical resonator is presented. Also, a method of miniaturizing the overall size of the resonator is demonstrated. This chapter will begin with obtaining the dimensions of a helical resonator given specifications and validating the work previously done in [20]. Then, an incorporation of surface mount tuning elements and ideas to make this device integratable with a future RF system are presented.

#### 2.2 Design Guidelines

First, preliminary conditions of what is desirable from a helical resonator must be defined as the dimensions are all functions of the unloaded  $Q$  and resonant frequency [15], [26]. It is determined to design a resonator operating approxi-

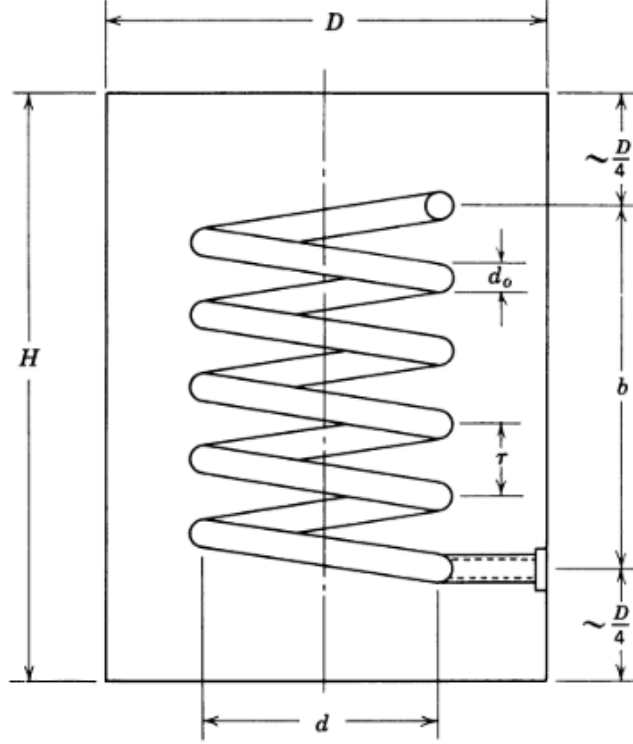


Figure 2.1: Helical resonator with a circular cross section defining parameters (from [26]).

mately in the middle of the VHF band, for this reason, the resonant frequency for this experiment is chosen to be 200 MHz. This is also a comparable operating frequency to the work presented in [20]. Additionally, another part of the preliminary conditions is having an unloaded  $Q$  of 1000. These parameters are chosen simply to obtain the initial helical dimensions. The  $Q$  will be reduced as the variable capacitive component is introduced in order to miniaturize the resonator. The expressions used to obtain the resonator dimensions found in [15], and that correspond to Fig. 2.1, are as follows:

$$Q_{un} = 50Df_o^{1/2} \quad (2.1)$$

$$0.45 < d/D < 0.6 \quad (2.2)$$

$$b/d > 1.0 \tag{2.3}$$

$$0.4 < d_0/\tau < 0.6 \text{ at } b/d = 1.5 \tag{2.4}$$

$$0.5 < d_0/\tau < 0.7 \text{ at } b/d = 4.0 \tag{2.5}$$

In order to determine the total number of turns:

$$N = 1900/(f_o D) \text{ turns} \tag{2.6}$$

$$d/D = 0.55 \tag{2.7}$$

where  $f_o$  is the operating frequency in megacycles (mc) per second (one megacycle is equivalent of one megahertz).  $D$  is the inner diameter of the cavity,  $H$  is the height of the inner cavity,  $b$  is the mean diameter of the helix, and  $b$  is the axial length of the coil. All dimensions are measured in inches. Using the preliminary conditions and the above expression, the following dimensions can be obtained:

$$D = \frac{1000}{50\sqrt{200}} = 1.414 \text{ in} \tag{2.8}$$

$$N = \frac{1900}{200D} = 6.7 \text{ turns} \tag{2.9}$$

For convenience and to proceed with an established standard, all measurements will be given in SI units from this point forward. Charts that approximate the optimum range for  $d/D$ ,  $b/d$ , and  $d_o/\tau$  can be found in [15], [26]. From this optimization and by solving for  $b$ , the initial volume can be determined. The inner diameter  $D$  is 36 mm and the axial length  $b$  is 20 mm, which allows for the following expressions to be used to solve for the internal volume of the resonator:

$$V = \pi r^2 h \tag{2.10}$$

where  $r = \frac{D}{2}$  and  $h = b + \frac{D}{2}$ .

$$V = \pi \left( \frac{D}{2} \right)^2 \left( b + \frac{D}{2} \right) \quad (2.11)$$

$$V \approx 38414 \text{ mm}^3 \approx 38.4 \text{ cm}^3 \quad (2.12)$$

### 2.3 Previous Work Validation

As a result, a resonator with 6.7 turns and a cavity diameter of approximately 36 mm, yields an internal volume of approximately 38 cm<sup>3</sup>. Although the resonator is significantly smaller than what a coaxial resonator would be at this frequency, it is still considerably large. The component contributing the most to the cavity size is the helix, which provides the inductive loading to the cavity. Heavy capacitive loading can be used to miniaturize the cavity, which offsets the inductance. This capacitive loading can be achieved by bending the top open-ended section of the helix towards the upper wall of the cavity, intentionally allowing a capacitive gap to exist between the two surfaces as seen in Fig. 2.2. As a result, the helix will experience a series capacitance as the two adjacent surfaces behave similarly to a parallel-plate capacitor as mentioned in [20]. This is where the miniaturization process happens. As the capacitive loading to the cavity is increased, the resonant frequency is reduced. The following expression demonstrates this relationship,  $f_o = 1/2\pi\sqrt{LC}$ . However, the resonant frequency is then brought back to the design resonant frequency of 200 MHz by reducing the size of the helix and cavity. In summary, the same resonant frequency of 200 MHz can be achieved with capacitive loading and an internal volume of only 8.6 cm<sup>3</sup>. This corresponds to a 22% volume size reduction.



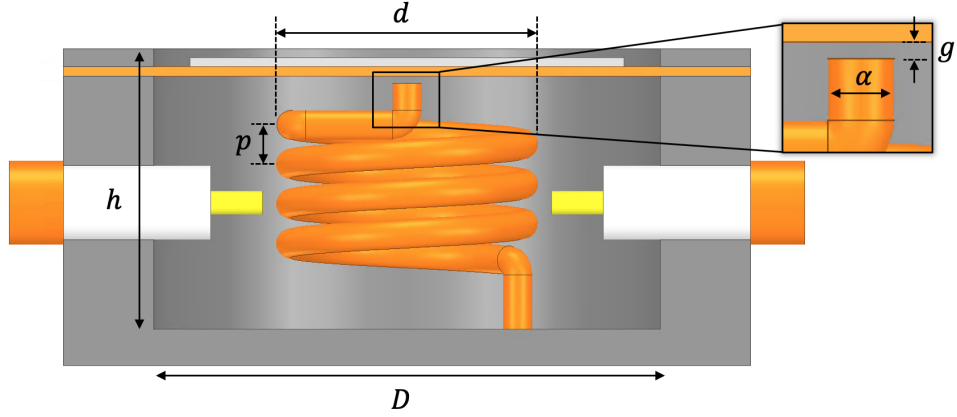


Figure 2.2: Internal view of the highly miniaturized tunable helical resonator with variable capacitive loading.

Compensating for the magnitude of the helical inductance (effectively reducing the helix size) by the capacitance should be carried out considering the effect on the resonator  $Q$ . The total resonator  $Q$  is composed of the  $Q$  provided by the cavity, helix, and capacitive element. Generally, the  $Q$  of the cavity and the helix are kept larger than the  $Q$  of the element providing the capacitance. Therefore, based on (2.13), the total  $Q$  of the resonator will be determined by the dominant factor, which is the  $Q$  of the capacitive elements.

$$\frac{1}{Q_{Total}} = \frac{1}{Q_{Cav}} + \frac{1}{Q_{Ind}} + \frac{1}{Q_{Cap}} \quad (2.13)$$

where  $Q_{Cav}$ ,  $Q_{Ind}$ , and  $Q_{Cap}$  are the quality factor values provided by the cavity, helix, and the element providing the capacitive loading, respectively. Considering the design guidelines, the final helical resonator was designed and optimized using Ansys High Frequency Structure Simulator (HFSS). The cross-sectional view of the weakly-coupled helical resonator, with all dimensions labeled, is shown in Fig. 2.2. Additionally, it can be seen that the RF-ports do not come in contact with the helical structure but rather have a separation. As this device is a building block for higher-order filters, this separation is

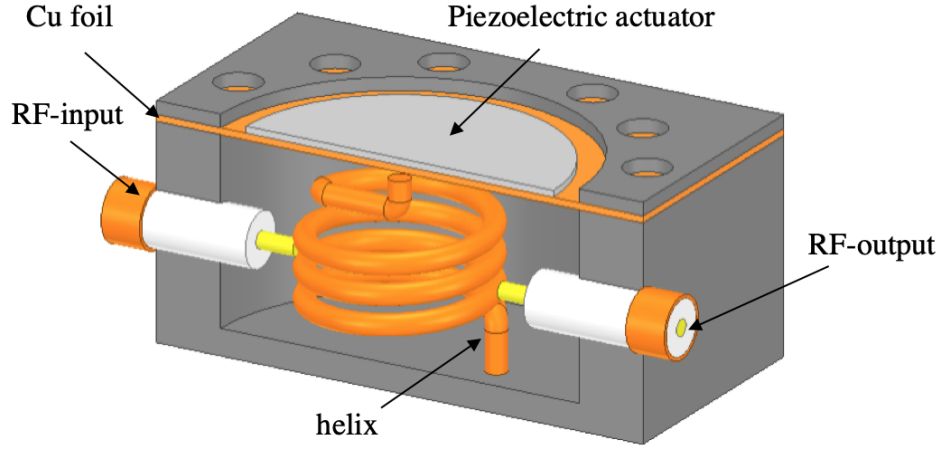


Figure 2.3: Conceptual model of the highly miniaturized tunable helical resonator with all components labeled.

to achieve a weakly-coupled resonator in order to extract the structure’s unloaded  $Q$  and tuning range. In other words, in order to extract the resonator’s electrical performances, the resonator needs to be isolated from external environment. Therefore, the main parameters for a helical resonator having a  $Q$  of 800, modeled with a piezoelectric actuator, are listed in Table 2.1.

Table 2.1:  
Highly Miniaturized Helical Resonator Design Parameters

Property	Value
Cavity diameter, $D$	28 mm
Helix diameter, $d$	14.4 mm
Cavity height, $h$	14 mm
Helix line diameter, $\alpha$	1.6 mm
Pitch, $p$	2.2 mm
Number of turns, $N$	3.4

A conceptual model of this resonator and the labeling of the different components can be seen in Fig. 2.3. The resonator is composed of a helix that is enclosed in an air-filled shielded cavity. The cavity cover is modeled as three parts, a copper foil, a piezoelectric actuator disk, and an anchor (uppermost) piece holding everything in place. The copper foil and piezo are adhered together which allows the copper foil to flex along with the piezo when biased. Lastly, the cavity has holes on its side walls to allow for input and output of the RF signal. From this design, simulations can be used to acquire the resonator's electrical performance.

### 2.3.1 Simulation

Using the ANSYS HFSS eigenmode and driven modal solver, various gap sizes can be simulated to observe not only the  $Q$  behavior but also the frequency-tuning range. This information gives insight into how much capacitance is being loaded to the cavity, which directly corresponds to the size and tuning range. Furthermore, the  $Q$  can be used to predict the loss of higher order filters realized by using this resonator. Initial resonator design with minimal details was performed in eigenmode simulation in order to obtain quick expectations of the fundamental resonator performance. For a representation that is closer to the fabricated device, a driven modal simulation is obtained as the design includes the impact of the feed ports. Therefore, the simulated  $Q$  and resonant frequency of the helical resonator are shown in Fig. 2.4 and gives an indication of the resonator characteristics. It is determined that a tuning range of approximately 200-400 MHz and an unloaded  $Q$  of 500-800 is expected by varying the gap size from approximately 2-50  $\mu\text{m}$ .

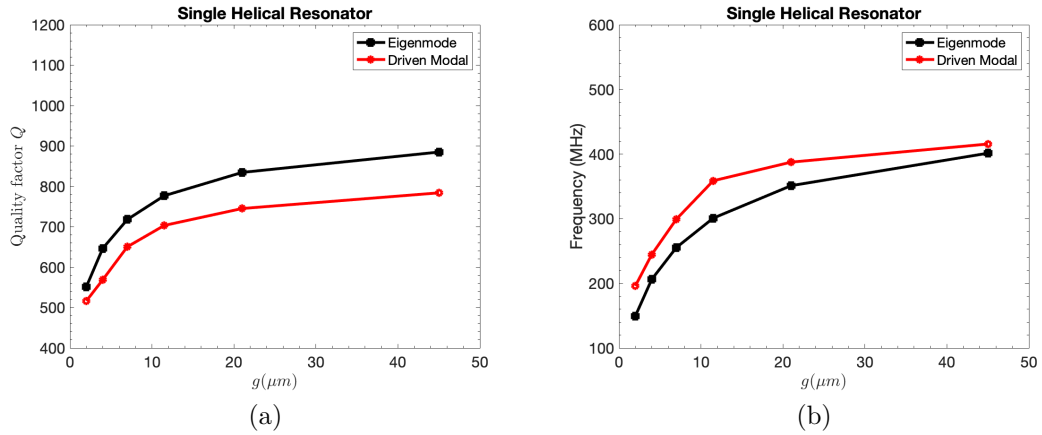
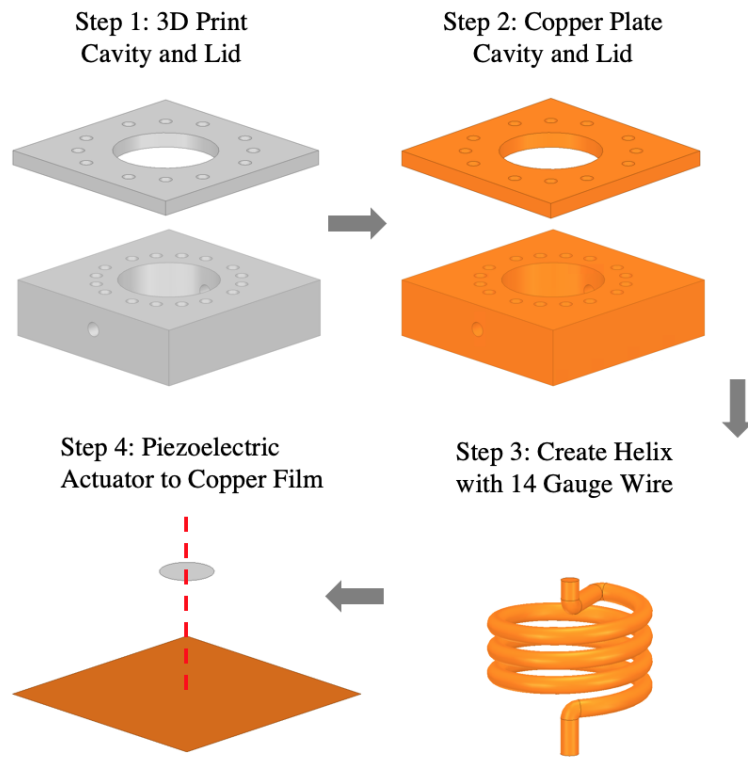


Figure 2.4: (a) Quality factor versus capacitive gap size and (b) resonant frequency versus capacitive gap size.

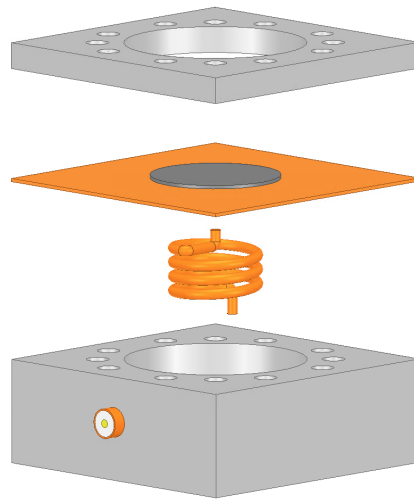
### 2.3.2 Fabrication and RF Measurements

3D-printing technologies are used to realize the cavity, the coil former, and the anchor piece. Further information regarding the type of printer used for this work, a method to obtain a 3D-print file from HFSS, and an overall process of how to metallize 3D-printed structures can be found in Chapter 5. In order to realize the helix, a 14 gauge copper wire is first wrapped in a socket in order to come in close proximity of the required diameter. Once the helix is formed, the 3D-printed coil former, seen in Fig. 2.6, is threaded into the helix in order to achieve the specific pitch. The piezoelectric disk actuator that was conveniently available in our facility is the PSI-5A4E from PIEZO SYSTEMS, which is intended to have a displacement of  $\pm 19.1 \mu\text{m}$  when the actuation voltage is swept from -180 V to +180 V. A brief overview of the fabricated process is provided in Fig. 2.5a and an exploded view model is shown in Fig. 2.5b.

One of the first measurements taken for this experiment was of the cavity



(a)



(b)

Figure 2.5: (a) Overview of the fabrication process and (b) exploded view of the highly miniaturized helical resonator.



Figure 2.6: Photograph of the 3D-printed coil former

without the helix. Because the cavity volume was significantly reduced, it is important to see the impact of the resonant frequency without the loading provided by the helix and piezo. Intuitively, a higher resonant frequency should be observed since removing the helix removes both the inductive and capacitive loading. Fig. 2.7, shows a comparison between simulated and measured results of the cavity without the presence of the inner helical structure. As can be seen, Fig. 2.7 shows very good agreement between simulated and measured results as there is a resonant frequency at approximately 14 GHz. It is interesting to note that a structure of size that resonates at 14 GHz (unloaded) will also resonate at 200 MHz (with loading). Fig. 2.8 shows the measured results of the helical resonator. Fig. 2.8 shows two vastly different results. The electrically tuned measurements shown in Fig. 2.8a have a significantly smaller tuning range than the mechanically tuned results shown in Fig. 2.8b. Upon investigation, it was determined that the piezo electric actuator that was used in this experiment was too small and the opening of the cavity lid was too large. Therefore, the piezo was not properly anchored to the cavity, resulting a minimum deflection when biased. In order to test this concept,

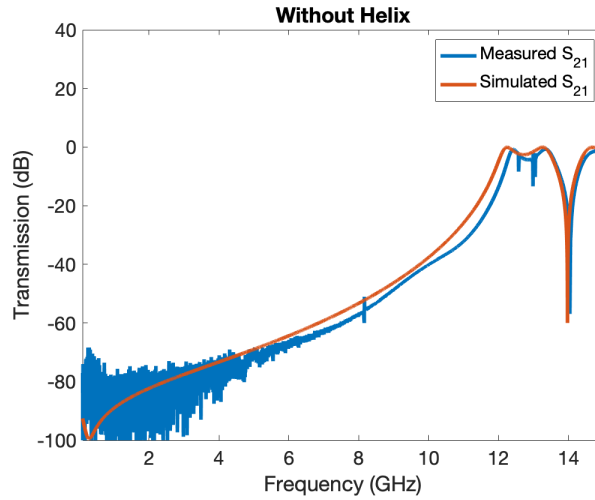


Figure 2.7: Comparison of the simulated and measured results of the cavity without the helix.

small nuts were used as weights to apply pressure on the top of the piezo. By mechanically reducing the capacitive gap size, the capacitive loading increases, which reduces the resonant frequency. Likewise, by pulling the piezo upwards or away from the cavity by sticking a piece of tape to the piezo and pulling away, the resonant frequency increases as the capacitive loading is reduced. This concept is verified in Fig. 2.8b. The original resonant frequency that can be seen in both Fig. 2.8a and Fig. 2.8b is approximately 420 MHz. By applying pressure to the piezo, the resonant frequency is brought down to approximately 355 MHz. Furthermore, by pulling the piezo away, the frequency is brought to approximately 440 MHz. From this, it is clear that everything is fundamentally working properly and can be validated. Capacitive values can be extracted from the simulated results and the unloaded  $Q$  can be extracted by measured results. Referring to Fig. 2.4b, it can be seen that by having a gap size of  $10 \mu\text{m}$ , a resonant frequency can be achieved. Using the following expression:

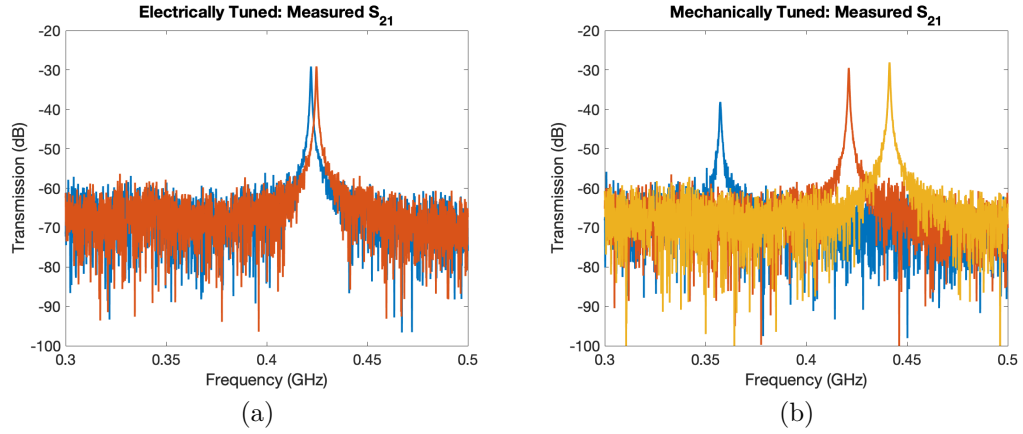


Figure 2.8: Measured results of (a) electrically tuning the resonant frequency and (b) mechanically tuning the resonant frequency .

$$C = \frac{\epsilon A}{d} \quad (2.14)$$

where  $C$  is the capacitance,  $d$  is the capacitive gap size, and  $A$  is the area of the parallel plate. In this case, the area of the 14 gauge wire will be used, which measures approximately 1.6 mm in diameter. Other parameters include  $\epsilon = \epsilon_o \epsilon_r$  where  $\epsilon_o = 8.85 \times 10^{-12}$  F/m and  $\epsilon_r = 1$ .

$$C = \frac{\epsilon_o \epsilon_r (\pi 0.8 \text{ mm}^2)}{10 \text{ } \mu\text{m}} \quad (2.15)$$

which results in a very obtainable capacitance value of 1.78 pF. Additionally, the range of capacitance that is required to realize a comparable frequency tuning range can be easily replaced by various other readily available components. This gives flexible options when comparing capacitive components for future work.



The unloaded  $Q$  is measured to be 562, 771, and 779 for the resonant frequencies corresponding to 355 MHz, 420 MHz, and 440 MHz respectively. The tuning concept of the resonator is validated, and the extracted  $Q$  from the simulated and measured results are in good agreement. This allows a path to explore other ways to facilitate the capacitive component providing the loading and potentially other ways to make this device integratable.

## 2.4 Proposed Design

The idea behind this work is to have a combination of a high  $Q$  resonator with rapid tuning surface mount components in order to completely eliminate all moving parts. Furthermore, the ultimate goal is to realize a highly miniaturized tunable helical resonator that is not only functional in terms of tunability, but also practical to modern RF systems by being able to integrate with future RF components. By using the same dimensions as in Section 2.3.2, a helical resonator using varactor diodes to achieve frequency tuning is presented in this section.

One of the benefits of using surface mount components, such as varactor diodes, is that they occupy minimal space. Another benefit is that it gives rise to the need of using a printed circuit board (PCB) as the varactors need to be fastened and the cavity needs a shielded cover. Additionally, it is desirable to stay away from connectors and develop practical new methods of coupling in to the helical structure while taking full advantage of the PCB. A conceptual model of the proposed helical resonator with a patterned PCB and varactor diodes is shown in Fig. 2.9 and Fig. 2.10.

It can be seen that the core components remain the same as the work shown in Section 2.3.2. Fig. 2.9 also demonstrates an equivalent circuit model

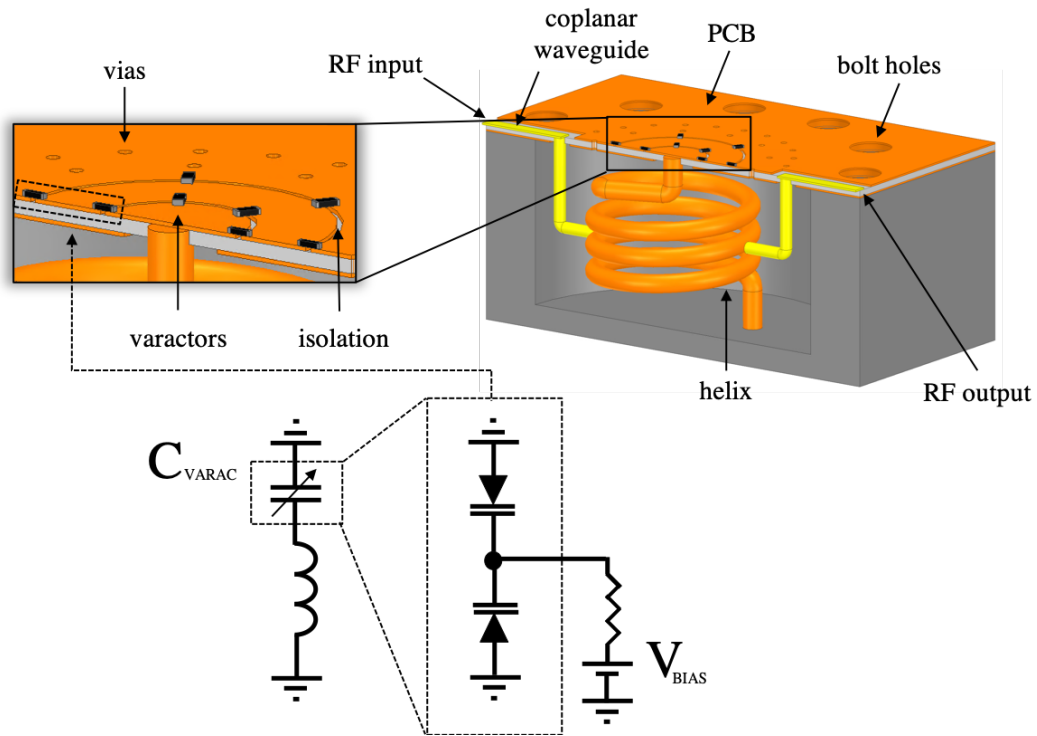


Figure 2.9: Conceptual model of the proposed miniaturized tunable helical resonator including an equivalent circuit of the resonator.

that represents each component that make up the proposed helical resonator. One of the main differences includes the absence of the SMA connectors. In the new model, it was found useful to incorporate coplanar waveguides on the top copper layer as a transition from the ports to the L-bar depicted as yellow traces in Fig. 2.9. It can also be seen that an L-bar tapped connection is used to complete the transition from the coplanar waveguide to the helix, providing the external coupling. As mentioned previously, designing a weakly coupled resonator is of interest as it allows to extract the resonator's electrical performances. Therefore, the L-bar is not tapped onto the helix but rather is placed adjacent near the helix as seen in Fig. 2.10. This minimizes the magnitude of coupling that is provided by the network analyzer. There is neither a precise measure for the separation between the L-bar nor is there for

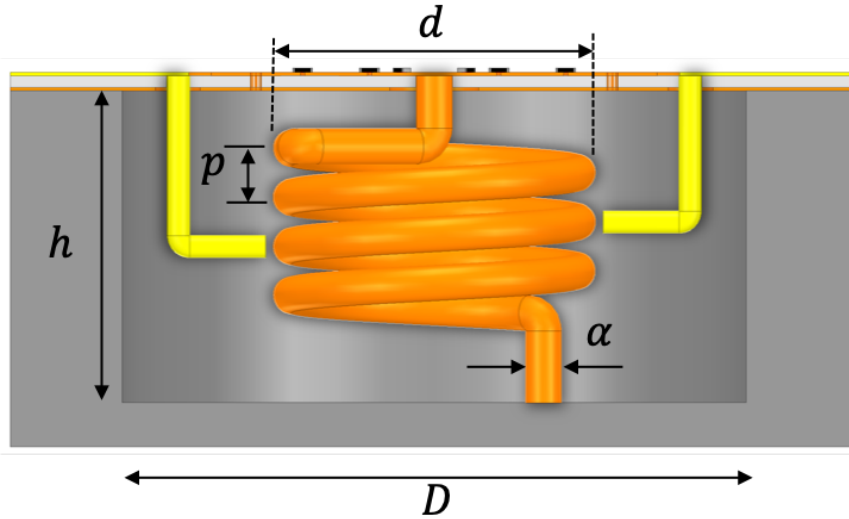


Figure 2.10: Internal view of the conceptual model of the proposed miniaturized tunable helical resonator.  $D = 28$  mm,  $d = 14.4$  mm,  $h = 14$  mm,  $\alpha = 1.6$  mm,  $p = 2.2$  mm, and the number of turns  $N = 3.4$ .

the length of the L-bar. As long as a weakly coupled response is achieved, the dimensions for the L-bar are arbitrary at this stage of the design. Furthermore, utilizing the L-bars provides an additional path of energy transfer which causes some interesting results that will be shown and discussed in Chapter 3.

Microwave Office, also referred to as AWR, is used to extract the coplanar waveguide dimensions based on the operating frequency and the PCB characteristics. For this study, the PCB that was chosen is a 0.508 mm-thick microwave laminate (RO4350B PCB from Rogers Corporation). Based on these dimensions, the gauge for the L-bar wire was chose to best fit with the means, which is 18 gauge. In order to obtain the final cavity cover, the PCB was processed with the following procedure. First, the vias and bolt holes are drilled using a LPKF, then copper plating to achieve ground connection between the top and bottom copper layers. Then, a mask was created using HFSS to proceed with a photolithography process in order to pattern the board with the coplanar waveguides and the copper isolation rings for the bi-

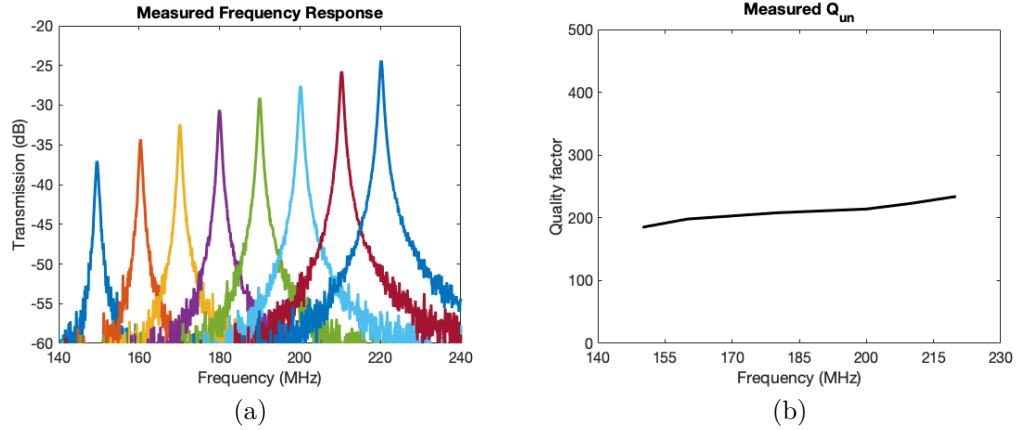


Figure 2.11: Measured response of the fabricated highly miniaturized tunable helical resonator at various states, (a) Transmission versus frequency response. (b) Extracted unloaded  $Q$  from measured S-parameters.

asing points as seen in Fig. 2.9. The types of varactors that were utilized to vary the capacitance are SMV1405-040LF by Skyworks Solutions, Inc. These varactor diodes provide a variable capacitance of 0.56-2.81 pF for a 0-30 V reverse biasing. The list of dimensions for a  $Q$  of 300 with varactors modeled as ideal capacitors are found in Table 2.1 or in the description in Fig. 2.10.

Fig. 2.11a shows the measured frequency response of the proposed helical resonator. It can be seen that the total tuning range from 150-220 MHz is achieved. It is important to note that even though there are only a number of states presented, the resonator is able to continuously tune across the tuning range. The highest level of transmission measures to be approximately -25 dB, which is sufficient to proceed with the unloaded  $Q$  extraction. Therefore, the unloaded  $Q$  associated with the tuning range is measured to be 185-234, as seen in Fig. 2.11b. This  $Q$  measurement maintains a relatively constant level throughout the frequency sweep and has good agreement with the simulated  $Q$ . Fig. 2.12 shows photographs of the fabricated miniaturized tunable helical

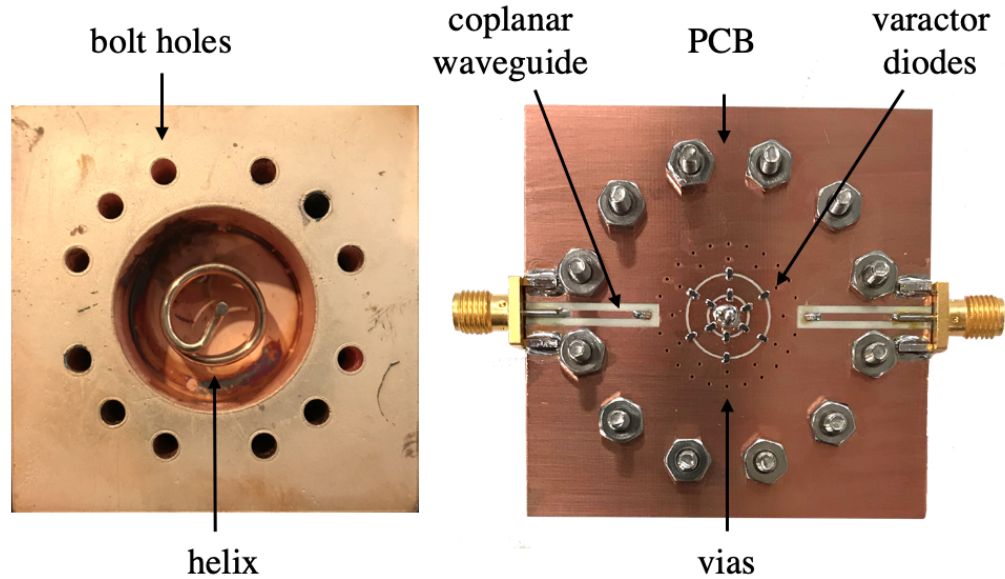


Figure 2.12: Photograph of the fabricated miniaturized tunable helical resonator with the cover off (left) and fully assembled (right).

resonator. In this photograph, it becomes easier to imagine how the top cover of the resonator can be utilized as a place to directly host future integration of RF component (amplifiers, mixers, etc.). Now that the proposed helical resonator is characterized, the design of higher order helical filters can take place.

## 2.5 Discussion on Capabilities & Improvements

All the parts that were used to realize the helical resonators in this chapter are used due to their availability in the Radar Innovations Laboratory. Therefore, the results of the helical resonator utilizing a piezoelectric disk actuator can be improved by obtaining a larger disk. The mechanical pressure that was applied produced a shift in resonant frequency, indicating that the smaller piezo was not well anchored. In other words, the piezo seemed to just float on the copper film. However, this issue can be resolved by using a piezo that

is approximately the same size as the cavity diameter. The closer in size the piezo is to the cavity, the better the anchoring. This allows the outer portion of the piezo to be in a fixed position near the edge of the cavity lid and allows the center portion of the piezo to freely deflect up or down.

For the helical resonator using varactor diodes, the tuning range can be increased by using other varactors that supply a larger capacitive span. Surface roughness is always a contributing factor to the overall performance. As the cavities of both resonators were 3D printed and copper plated, the  $Q$  has the potential to be improved by using a copper cavity.

## 2.6 Conclusion

A highly miniaturized, tunable helical resonator is presented. PCBs are employed to facilitate the cavity lid, which allowed a place to fasten the varactors and patterning of the coplanar waveguides. It was shown that PCBs also provides a place to host future integration of RF components directly on the top copper layer making this device a strong candidate for modern integrated system. Furthermore, a new method of coupling into the helical resonator utilizing an L-bar is presented. The proposed helical resonator measured a continuous tuning resonant frequency of 150-220 MHz with an unloaded  $Q$  of 185-234.

## Chapter 3

### Tunable Second Order Helical Filters

#### 3.1 Introduction

In order to better understand the capabilities of the proposed concept of rapid continuous tunability in a miniaturized helical resonator, a second-order tunable helical filter is presented as a proof-of-concept demonstrator [27]. This is a direct continuation of the work presented in Chapter 2. Starting, with standard Butterworth low-pass prototype  $g$ -coefficients and ending with measured results, this chapter will go step by step in explaining the work of the realization of a 4% tunable bandpass filter operating at 200 MHz. Upon obtaining the measured results, the performance of this filter will be compared to traditional ideal filters such as a second-order Butterworth and Chebyshev filter. Although this chapter discusses a second-order filter, the guidelines presented here can be applied to achieve higher order filters.

### 3.2 Helical Resonator Filter Design

For the work presented here, the external quality ( $Q_{ext}$ ) and resonator coupling coefficients ( $K_{1,2}$ ) are calculated using the Butterworth lowpass prototype in [28]. ( $Q_{ext}$ ) determines the feeding position of the filter to ensure a chosen fractional bandwidth.  $K_{1,2}$  is responsible for the inter-resonator coupling and also contributes to the bandwidth and overall shape of the response. By using the filter synthesis in [3] and calculations made in MATLAB, the  $g$ -coefficients are as follows:

$$g_0 = 1$$

$$g_1 = 1.4142$$

$$g_2 = 1.4142$$

$$g_3 = 1$$

When a single resonator has been previously characterized, the order of the filter is known, and the fractional bandwidth of the design is known, the insertion loss of higher order filters can be predicted by using the following expression provided by [29].

$$IL = \frac{17.372}{\Delta Q_u g_1} \text{ dB} \quad (3.1)$$

$$IL = \frac{17.372}{0.04 \times 200 \times 1.4142} = 1.75 \text{ dB} \quad (3.2)$$

where  $\Delta$  is the fractional bandwidth and  $Q_u$  is the unloaded quality factor. The coupling matrix  $M_{i,j}$  values are then calculated and converted to coupling



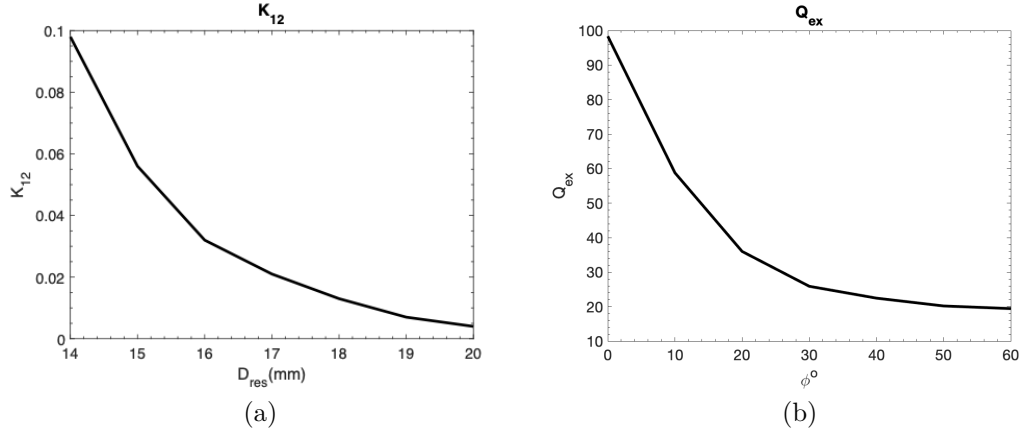


Figure 3.1: Calculated relationship between (a)  $K_{1,2}$  and  $D_{res}$  and (b)  $Q_{ext}$  and  $\phi$ .

coefficients  $k_{i,j}$  as follows:

$$M_{S,1} = \frac{1}{\sqrt{g_0 g_1}} = 0.8409$$

$$M_{1,2} = \frac{1}{\sqrt{g_1 g_2}} = 0.7071$$

$$M_{2,1} = M_{1,2} \text{ and } M_{2,L} = M_{S,1}$$

$$K_{1,2} = \Delta M_{1,2} = 4\%(0.7071) = 0.028284$$

The next step is to use the  $g$ -coefficients to obtain a targeted value for the  $Q_{ext}$ .

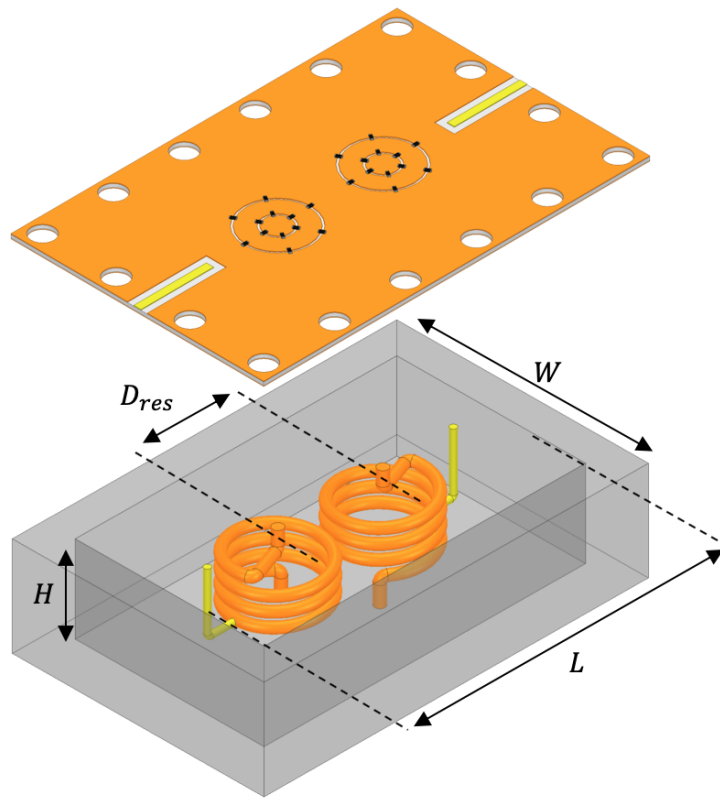
$$Q_{ext} = \frac{g_0 g_1}{\Delta} = \frac{1.4142}{0.04} = 35.35$$

HFSS is then utilized to optimize the model and to convert the  $K_{1,2}$  value into a physical dimension that measures the distance between the resonators,  $D_{res}$ . The  $Q_{ext}$  is also converted into a physical property by rotating the helix

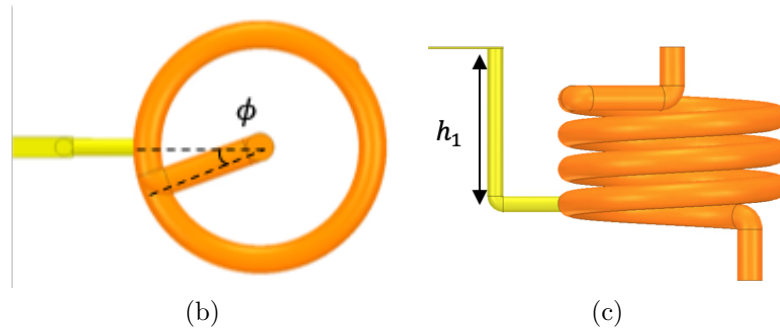
Table 3.1:  
Second-Order Filter Design Parameters

Property	Value
Cavity length, $L$	51 mm
Cavity width, $W$	30 mm
Cavity height, $H$	14 mm
Wire diameter, $\alpha$	1.6 mm
Pitch, $p$	2.2 mm
L-bar length, $h_1$	9.2 mm
Resonator diameter, $d$	14.4 mm
Resonator separation, $D_{res}$	16.6 mm
Resonator rotation, $\phi$	20°
Number of turns, N	3.4

about its own axis and changing where the L-bar is tapping into the helix. Furthermore, the relationship between  $K_{1,2}$  and  $D_{res}$  and between  $Q_{ext}$  and  $\phi$  are demonstrated in Fig. 3.1a and Fig. 3.1b respectively. Based on Fig. 3.1, initial dimensions are obtained. The final dimensions for the designed second-order helical resonator filter after optimization are listed in Table 3.1. The 3D model of the designed filter along with the definitions of all parameters are shown in Fig. 3.2.



(a)



(b)

(c)

Figure 3.2: Model of the miniaturized tunable helical resonator filter. (a) Showing dimensions of the different parts of the filter assembly. (b) Defining the reference point for the L-bar tap point. (c) Showing the location where the L-bar taps to the helix.

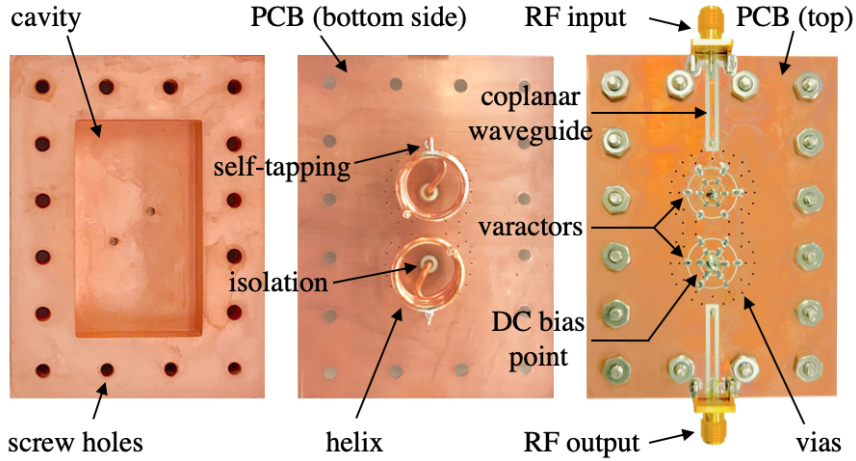


Figure 3.3: Photograph of the fabricated prototype of the second-order tunable helical resonator filter.

### 3.3 Experimental Validation

The cavity was 3D printed and copper plated while the helical structures are realized by wrapping 14 gauge wire to form a helix. The cavity lid was realized by patterning a 0.508 mm-thick microwave laminate (RO4350B from Rogers Corporation), similarly done in Chapter 2. Additionally, the variable capacitive loading was achieved by utilizing varactor diodes SMV1405-040LF from Skyworks Solutions. Unlike the intentionally imposed gap between the L-bar and resonator for the weakly-coupled design, shown in Fig. 2.10, the L-bar taps directly to the helical resonators in the filter design, as seen in Fig. 3.2c. A photograph of the fabricated helical filter is shown in Fig. 3.3.

The measured S-parameters of the fabricated tunable helical filter, tuned at different states, are shown in Fig. 3.4. It can be observed in a zoomed in plot in Fig. 3.5a that the filter response exhibits Butterworth-like qualities in the passband across the whole tuning range (no ripples in the passband and similar input reflection behavior). The measured insertion loss is 0.9-1.3 dB throughout the tuning frequency range of 170-230 MHz as seen in Fig. 3.5a.

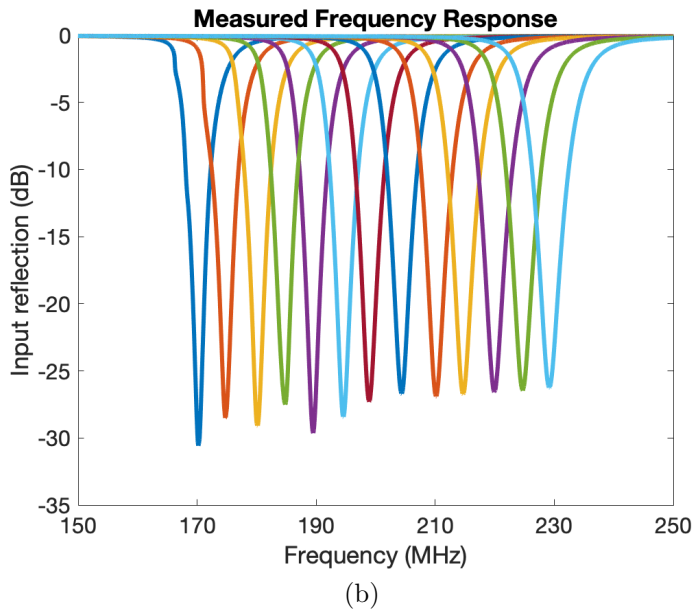
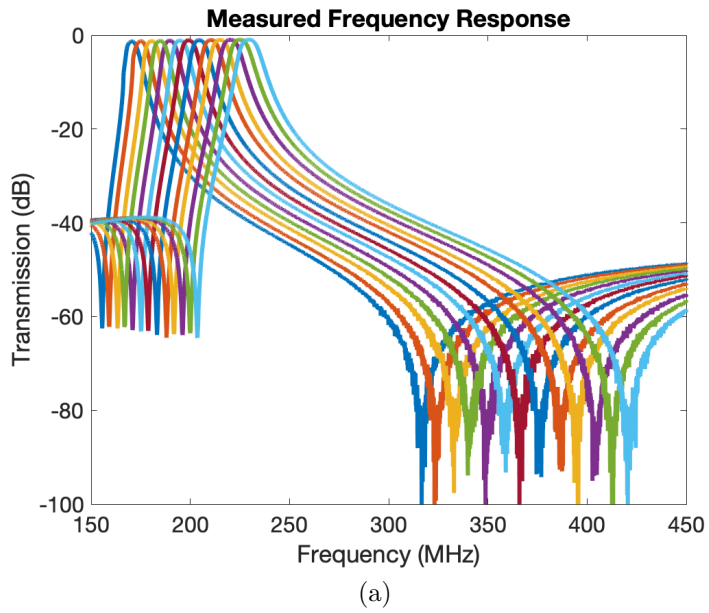
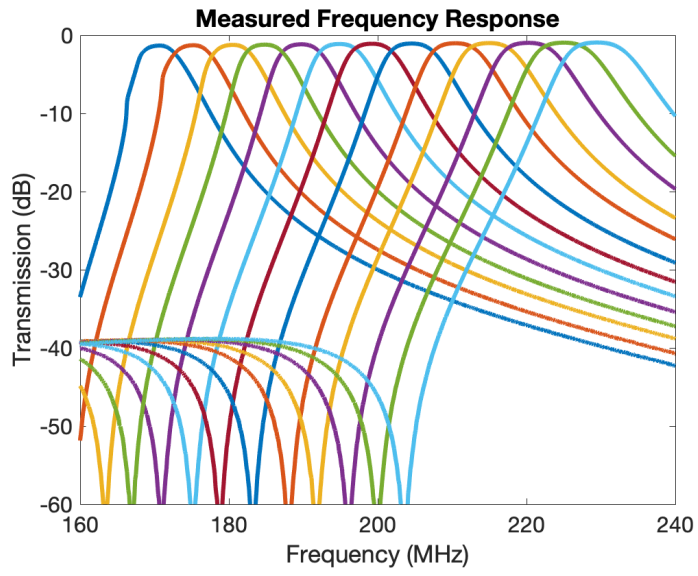
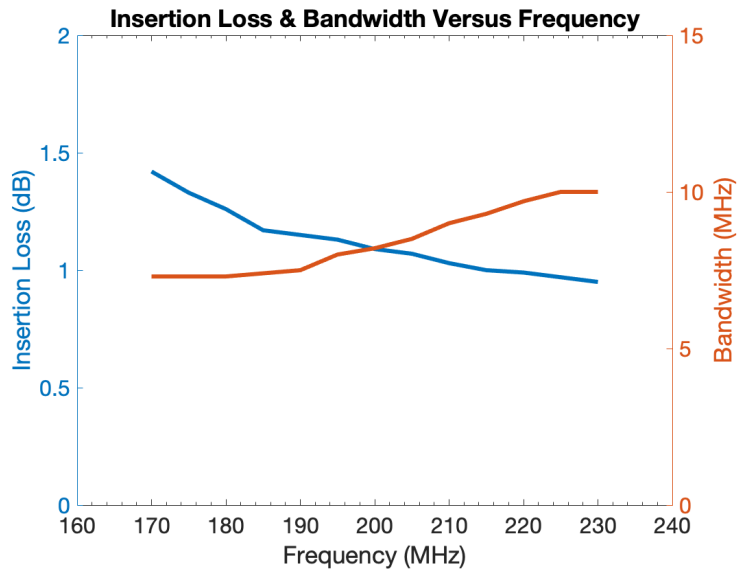


Figure 3.4: Measured frequency responses of the fabricated tunable helical resonator filter at various capacitance states. (a) Transmission response versus frequency. (b) Input reflection response versus frequency.



(a)



(b)

Figure 3.5: (a) Zoomed in plot of the transmission response versus frequency. (b) Relationship between the insertion loss as a function of frequency.

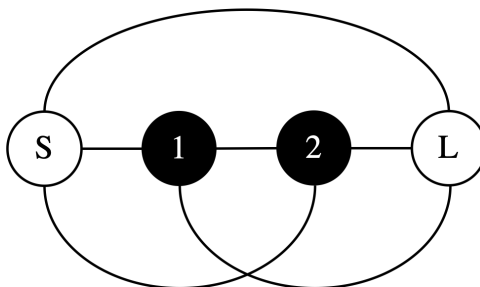


Figure 3.6: Proposed coupling diagram of the tunable helical filter.

The measured insertion loss is lower than the insertion loss of 1.75 dB that was predicted using (3.1). Furthermore, the relationship of the insertion loss and bandwidth as a function of frequency is shown in Fig. 3.5b. In addition, the input reflection maintains a fairly constant level throughout the tunable frequency range.

Also, a very interesting result that is seen in Fig. 3.4a is that two TZs can be observed, one on each side of the passband. To explain the significance of this result, this helical filter has a second-order inline configuration. Filters that exhibit these characteristics typically have cross coupling in a staggered configuration. However, the direct tapping mechanism that was employed to facilitate external coupling, provides additional paths for energy transfer and self compensates for matching. Therefore, the proposed coupling diagram illustrating the additional paths of energy transfer is shown in Fig. 3.6. The left most TZ is due to the source-to-load coupling. The right most TZ is a combination of the source-to-resonator-one coupling and the resonator-two-to-load coupling. To further explain this phenomenon, a circuit design in AWR was used to confirm the cause of these TZs. Fig. 3.7a shows the schematic that was used in AWR and Fig. 3.7b shows the frequency response of AWR and HFSS. Fig. 3.7b shows very good agreement between the results obtained from the HFSS and AWR simulations. This result confirms the coupling interaction

seen in Fig. 3.6.

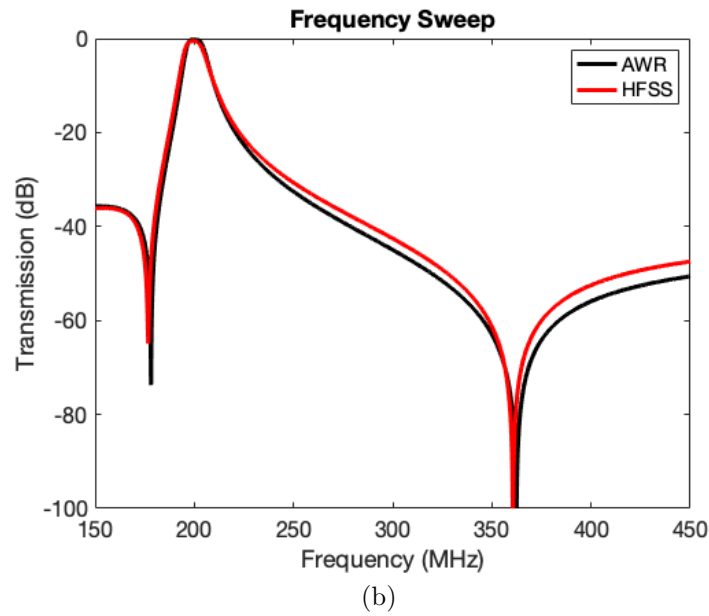
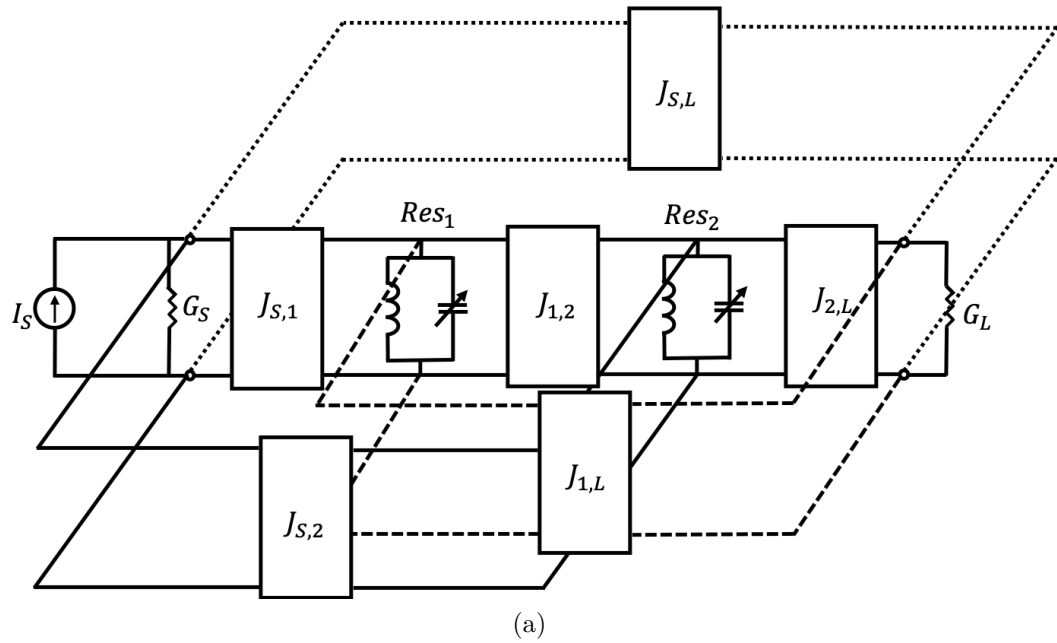
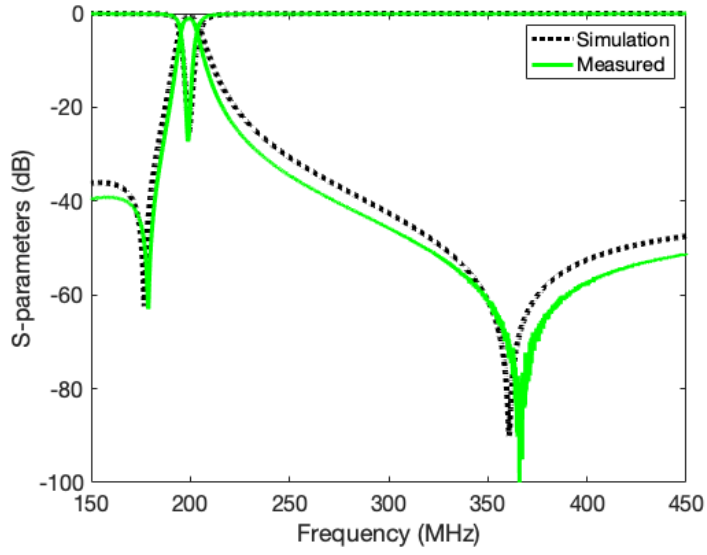
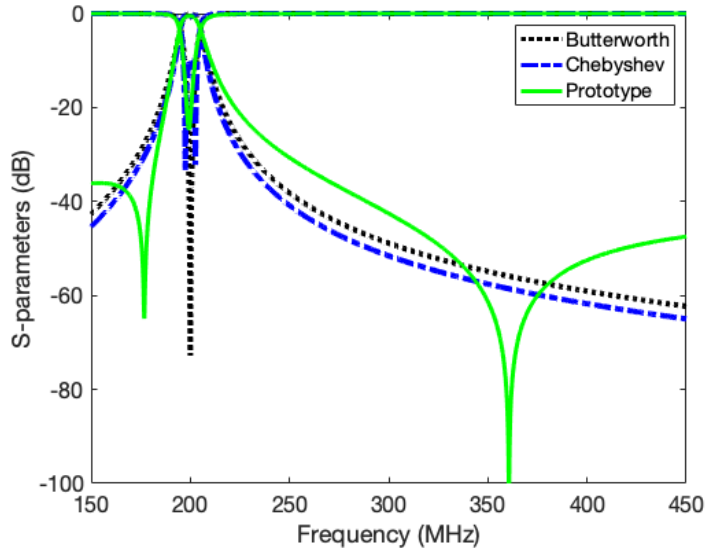


Figure 3.7: (a) AWR schematic implementing additional paths of energy transfer causing two transmission zeros and a (b) frequency response of the AWR schematic and HFSS results overlaid at a sample of 200 MHz.





(a)



(b)

Figure 3.8: (a) Comparison of simulated and measured S-parameter responses at 200 MHz. (b) Comparing second-order bandpass filter responses utilizing Butterworth, Chebyshev, and simulated results of the proposed prototype helical filter at 200 MHz.

A measured sample at 200 MHz was taken from the fabricated helical filter to make a direct comparison with the simulated results and is shown in Fig. 3.8a. It can be observed that there exists good agreement between simulation and measured response. To make an even further comparison, Fig. 3.8b shows a plot of a second-order bandpass filter featuring Butterworth and Chebyshev responses along with the simulated response from the design in Fig. 3.2, all centered at 200 MHz. Even though the bandwidths for a Butterworth filter and Chebyshev filter are defined differently, a 3-dB bandwidth was used for all filters in this comparison, for better visualization purposes. It can be seen from Fig. 3.8b that the transmission zero on the lower side provides a better rejection than the compared counterparts. The transmission zero that is observed at the higher side is due to source-load coupling and can be manipulated for a better rejection.

### **3.4 Discussion on Capabilities & Improvements**

One of the areas that can be improved is to match the tuning range of the resonator that was characterized. As reported in Chapter 2, the tuning range is 150-220 MHz and the tuning range for the second-order filter that is presented in this chapter is 170-230 MHz. As the varactor diodes are extremely small, it is likely that not all of them made a solid electrical connection when soldered. Another likely possibility may have taken place when the biasing applied to the varactors approaches 0 V, or when the capacitance reaches a maximum. During this portion of extracting measurements, the response is very sensitive and the resonator poles are no longer synchronized. This phenomenon can be observed in Fig. 3.8a, and a method to reduce or eliminate this affect is to use a power supply that is able to filter out the noise.

Another area of improvement is manipulating the TZs to improve the rejection of the filter. The cause of each TZ are described and demonstrated using AWR. Further investigation needs to take place in the HFSS model in order to understand how it affects the other parameters. Having a better understanding will enable the capability to steer the TZ that is on the right side of the pass band closer, which brings significant advantages to the rejection.

### **3.5 Conclusion**

In this chapter, a novel concept of tuning miniaturized helical resonator filters using varactor diodes is presented for the first time. Coupling into the helical resonator filter using coplanar waveguides, which allows for transmission zeros on both sides of the passband, is also presented. The proposed method of implementing the tuning elements on a PCB allows for integration of RF components directly on the top cover of the filter. This work is a direct continuation of the helical resonator that was fabricated for characterization in Chapter 2. A second-order helical resonator bandpass filter was also fabricated and tested for validation. The helical filter achieved a continuous tuning center frequency of 170-230 MHz, an insertion loss of 0.9-1.3 dB, and a fractional bandwidth of 4%.

## Chapter 4

### Fully Reconfigurable Filters

#### 4.1 Introduction

In recent years, there has been a concentrated amount of effort in developing compact and tunable filter devices for intelligent microwave systems. Tunable filters are often preferred over bulky switched filter banks as they tend to occupy less space while out-performing at a lower cost. Much of the research has been done on bandpass filters with center-frequency agility as mentioned in Chapter 1. However, as the microwave spectrum continues to overpopulate, filters with fully reconfigurable capabilities are increasingly desirable. Therefore, in this chapter, a method of incorporating the second-order tunable helical filter presented in Chapter 3 with additional tuning elements will be presented. This work will demonstrate that having control over the external coupling, inter-resonator coupling, and resonant frequency can produce a filter with fully reconfigurable capabilities by controlling the filter's insertion loss, bandwidth, and center frequency, respectively.

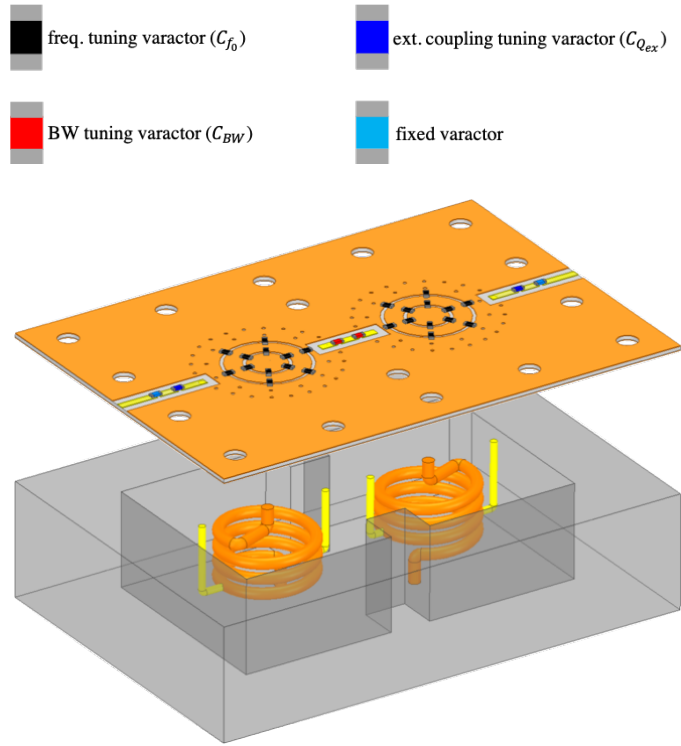
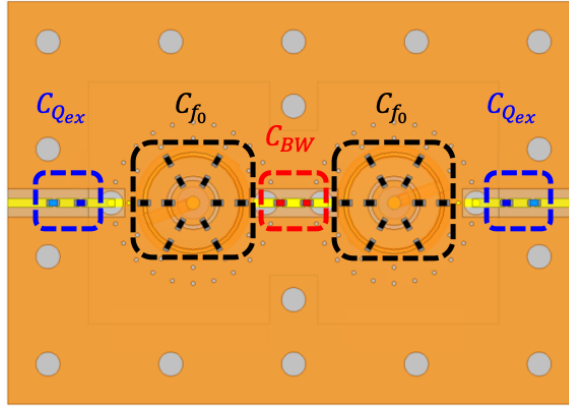


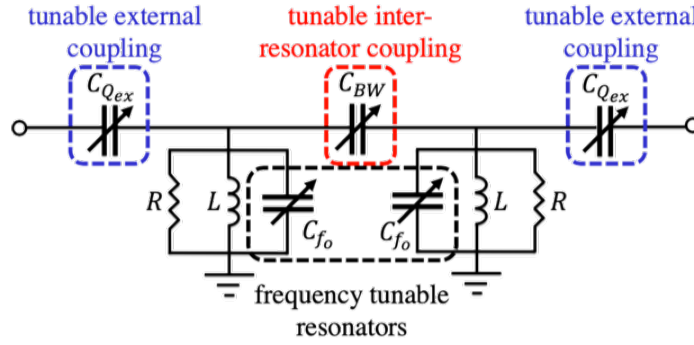
Figure 4.1: Conceptual model of the fully reconfigurable miniaturized helical resonator filter with labeled varactor diodes.

## 4.2 Design and Simulation

In order to control the inter-resonator coupling, a similar approach of utilizing the L-bar will be used. With the use of coplanar waveguides, the L-bar is connected on each side and tapped to its corresponding helix as seen in Fig 4.1. The bandwidth can be tuned by inserting varactor diodes in series with the coplanar waveguide trace. This configuration enables the concept of tuning the electrical length of the trace, therefore tuning the inter-resonator coupling. The same concept can be applied to the coplanar waveguide traces that control the external coupling. Fig 4.1 shows an exploded model of the design as well as reference to the different varactors. Additionally, Fig. 4.2 provides a top



(a)



(b)

Figure 4.2: Conceptual design model of proposed reconfigurable helical filter (a) top view highlighting the roll of each group of varactors and (b) equivalent circuit representation.

view design image, highlighting the roll of each group of varactor diodes.

Similar to the procedure shown in Chapter 3, the  $Q_{ext}$  and  $K_{1,2}$ , are calculated using the Butterworth lowpass prototype. A second-order 4% bandpass filter was fabricated and measured as a proof-of-concept demonstrator. The list of all the final dimensions are provided in Table 4.1 and the new parameters for the additional L-bars are defined in Fig. 4.3.

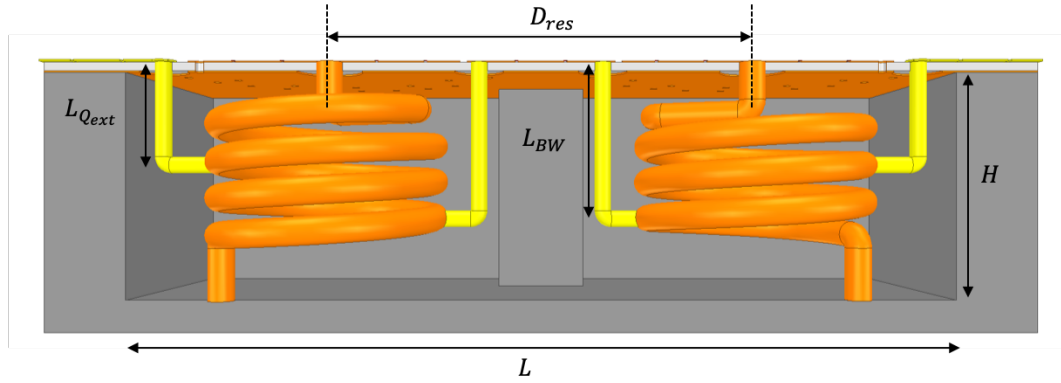
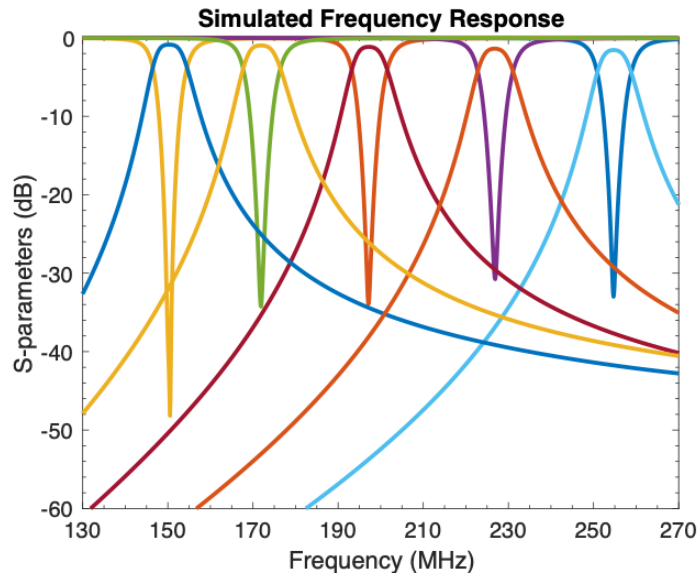


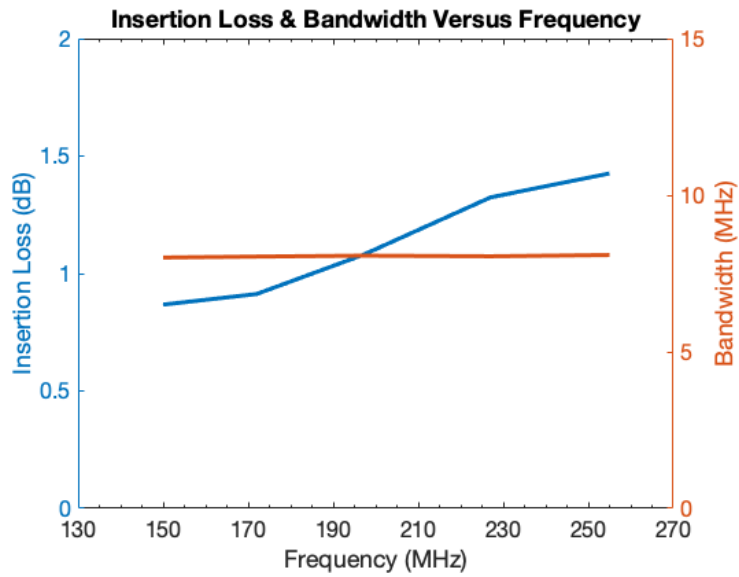
Figure 4.3: Internal view of the proposed helical filter defining new parameters.

Table 4.1:  
Fully Reconfigurable Miniaturized Filter Design Parameters

Property	Value
Cavity length, $L$	51 mm
Cavity width, $W$	30 mm
Cavity height, $H$	14 mm
Wire diameter, $\alpha$	1.6 mm
Pitch, $p$	2.2 mm
$Q_{ex}$ L-bar length, $L\text{-bar}_{Q_{ext}}$	5.81 mm
$BW$ L-bar length, $L\text{-bar}_{BW}$	9.11 mm
Resonator diameter, $d$	14.4 mm
Resonator separation, $D_{res}$	26 mm
Resonator rotation, $\phi$	160°
Number of turns, $N$	3.4



(a)



(b)

Figure 4.4: (a) Simulated frequency response of the fully reconfigurable helical filter showing an example of having constant absolute bandwidth of 8 MHz throughout the sweep. (b) Simulated relationship between the insertion loss and bandwidth with respect to the frequency sweep.



Fig. 4.4a shows the simulated frequency response of the proposed filter. It can be shown that from the initial design, the fractional bandwidth of 4% is maintained throughout the entire sweep. Additionally, the shape of the passband maintains a very nice and flat shape. The relationship between the insertion loss and the bandwidth is shown in Fig. 4.4b.

### 4.3 Experimental Validation

Fig. 4.5 shows the fabricated helical filter. Similar to the other devices reported in this work, the cavity is 3D-printed and copper plated. The PCB process is the same with the exception of the isolation points in the coplanar waveguides for the new set of varactor diodes. The varactors used for bandwidth tuning are the same as the ones used in Chapter 3, while the varactors used for external coupling are the SMV1236-079 from Skyworks Solutions, providing a variable capacitance of 3.80-26.75 pF for a 0-15 V reverse biasing. Additionally, to avoid a floating voltage, a fixed capacitor is placed to make the connection between the ports and the biasing point for the external coupling. A diagram that helps visualize this explanation is shown in Fig 4.1.

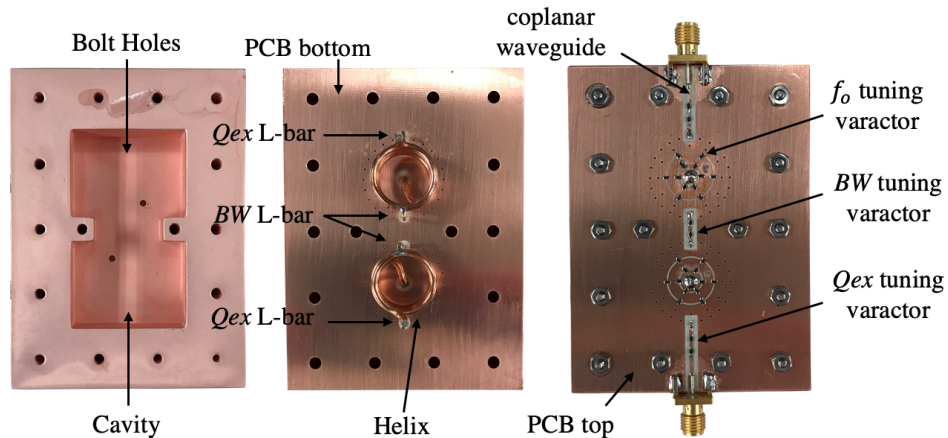
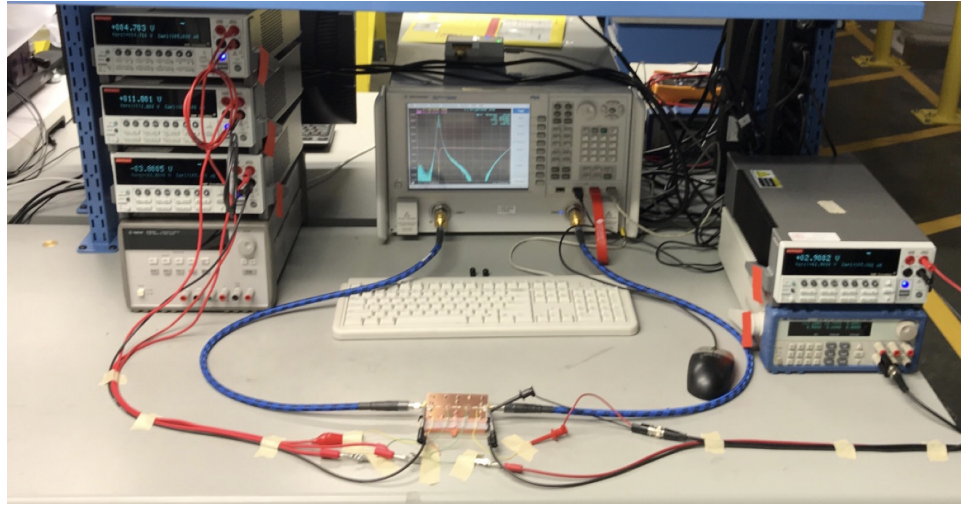
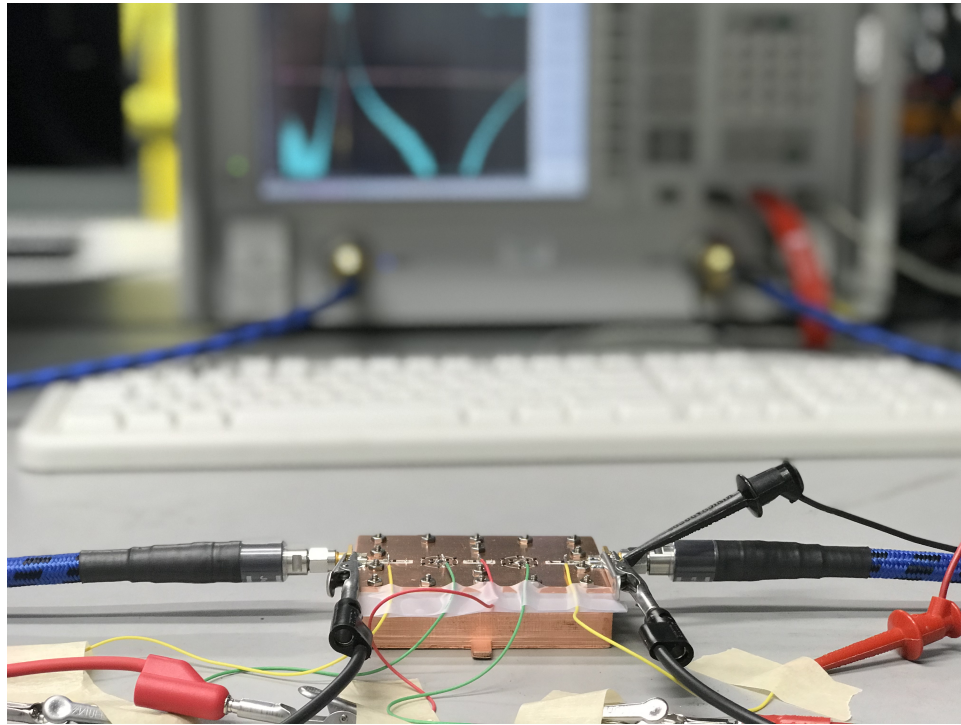


Figure 4.5: Photographs of the fabricated fully reconfigurable filter.



(a)



(b)

Figure 4.6: Photograph of the setup prior to obtaining measurements showing (a) all the power supplies that were required for tuning and a (b) zoomed in photograph of the filter.

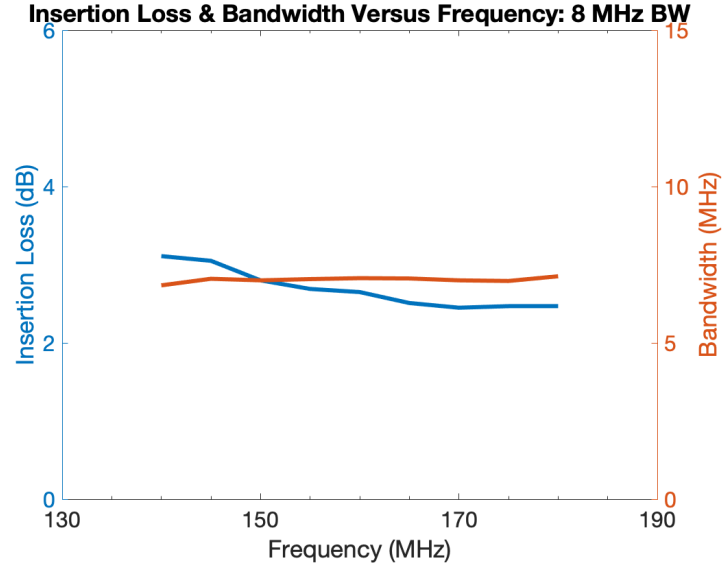
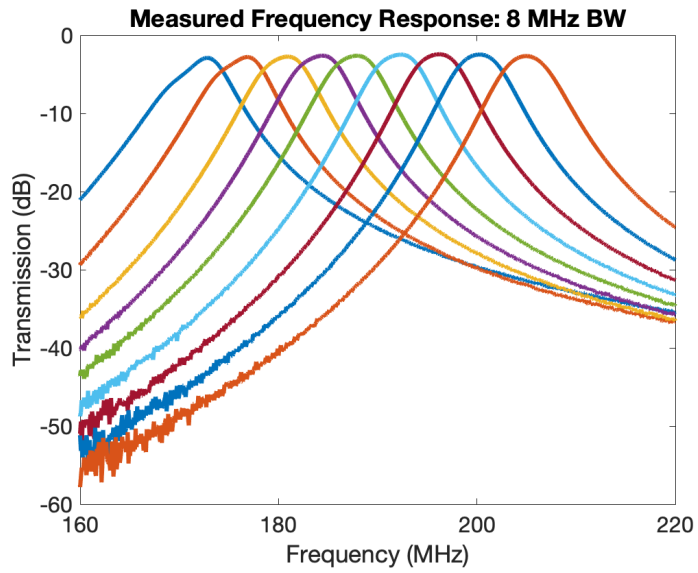
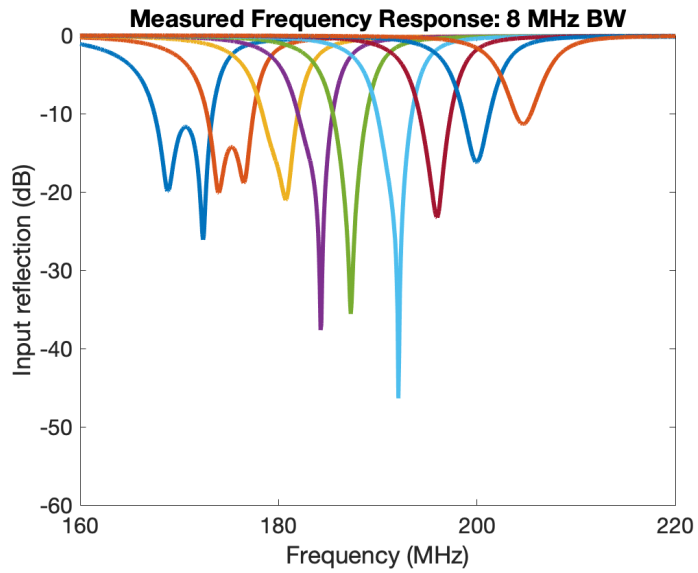


Figure 4.7: Measured behavior of insertion loss and bandwidth versus frequency demonstrating constant absolute bandwidth of 8 MHz.

Photographs of the measurement setup showing the fabricated filter connected to the network analyzer is shown in Fig. 4.6. As seen in Fig. 4.8, the measured results of the reconfigurable helical filter achieves a continuous sweep with a constant absolute bandwidth of 8 MHz. The tuning range is measured to be from 140-180 MHz and the associated insertion loss is 2.35-3.11 dB. Fig. 4.7 shows the measured relationship of the insertion loss and bandwidth as a function of frequency regarding the measured results seen in Fig. 4.8 . It can also be seen that the filter maintains a relatively nice shape in the band pass throughout the sweep. Also, to assist in making the claim of achieving reconfigurability, Fig. 4.9-4.12 demonstrate how the same filter can achieve a constant absolute bandwidth of 10 MHz and a constant fractional bandwidth throughout the sweep. An important note to mention is that no physical or mechanical change was required to accomplish this feature, only a bias voltage (electrical) change applied to the varactors was made.

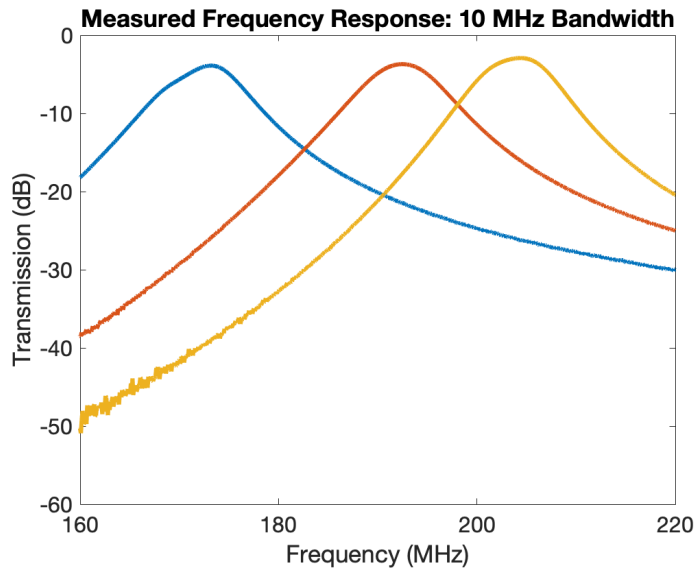


(a)

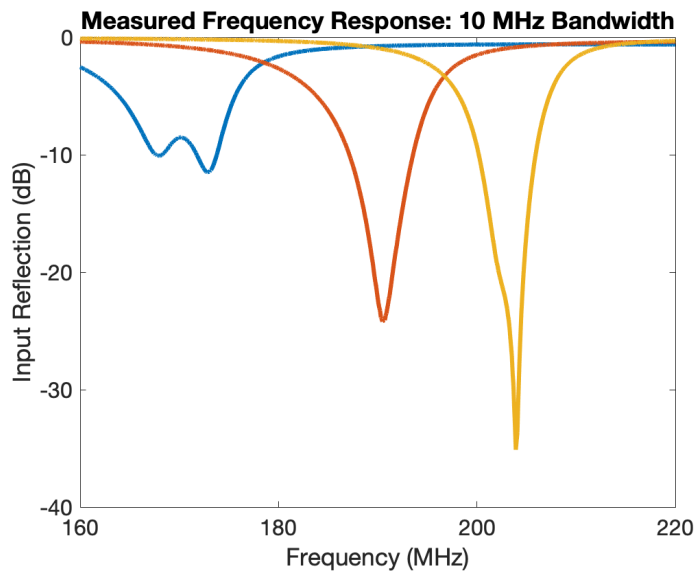


(b)

Figure 4.8: Measured results of the proposed fabricated reconfigurable filter demonstrated with 8 MHz absolute bandwidth across the whole tuning range with the (a) transmission versus frequency and (b) input reflection versus frequency.

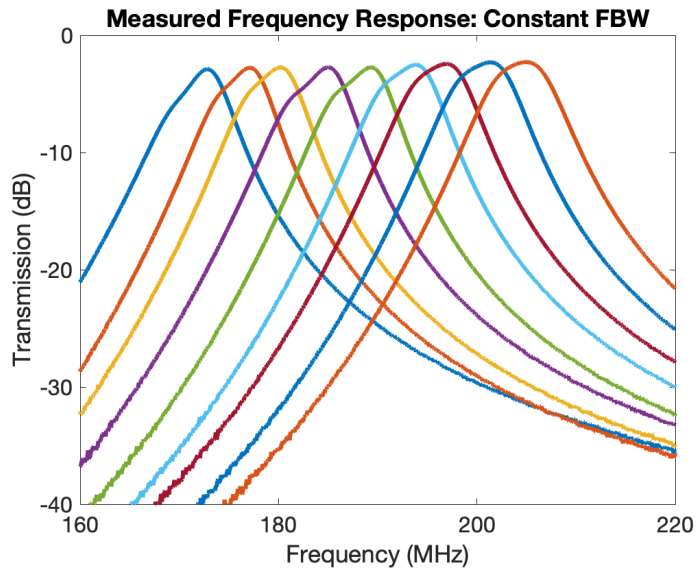


(a)

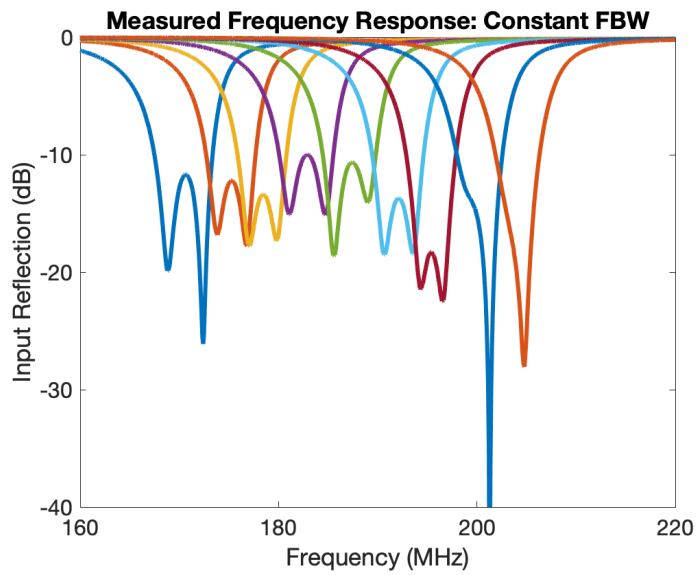


(b)

Figure 4.9: Measured results of the same fabricated reconfigurable filter with various sample of 10 MHz absolute bandwidth (a) transmission versus frequency and (b) input reflection versus frequency.



(a)



(b)

Figure 4.10: Measured results of the same fabricated reconfigurable filter demonstrating constant fraction bandwidth with (a) transmission versus frequency and (b) input reflection versus frequency.

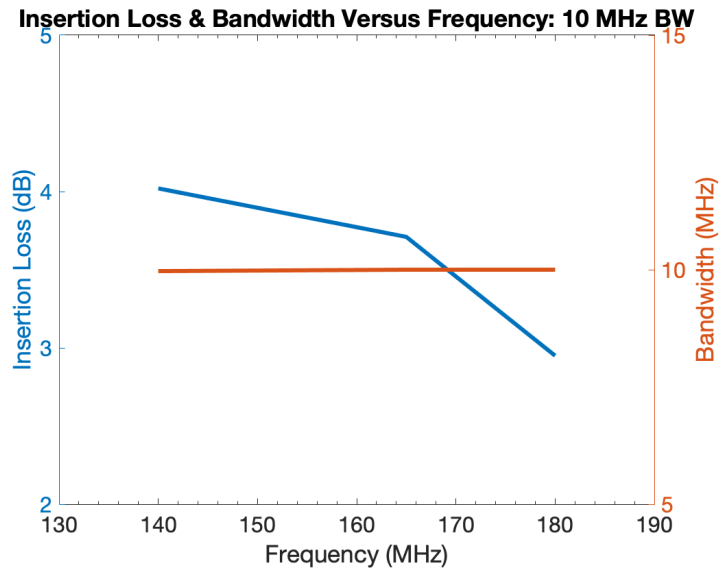


Figure 4.11: Measured behavior of insertion loss and bandwidth versus frequency from the results demonstrating constant absolute bandwidth of 10 MHz.

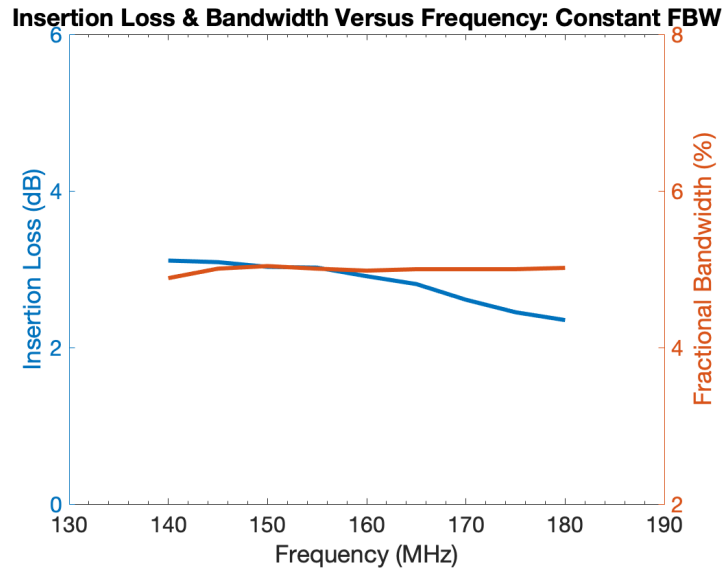


Figure 4.12: Measured behavior of insertion loss and bandwidth versus frequency from the results demonstrating constant fractional bandwidth.

## 4.4 Discussion on Capabilities & Improvements

Some of the areas that can improve are the tuning range and the shape of the pass band. The tuning range of the proposed reconfigurable filter was measured to be from 140-180 MHz. There were some complications during the fabrication process, specifically in the placement of the helices. These complications required drilling of new holes in the cavity after the cavity had been put through a copper-plating process. Furthermore, the method in which the filter is assembled, the electrical connection of the helix and inner cavity wall depends on the pressure of the helix wire as it is pushed through a hole in the cavity. When the new holes in the cavity are not copper plated, there are too many uncertainties to determine if the helices are making a solid electrical connection with the inner cavity walls.

One way to mitigate this issue is to fabricate the cavity without a side wall, leaving exposure to hard-to-reach places underneath the helices, where the solder joints are located. This method enables and visually ensures that a solid electrical connection is made. Another idea that has potential for a successful fabrication is by 3D-printing the cavity and helices as one solid piece. Not only is the issue regarding placement of the helices eliminated (as the helix and cavity are printed as a stand-alone piece), but the 3D-printed structure would be put through a copper-plating process as a whole, which would ensure a solid electrical connection.



## 4.5 Conclusion

The concept of having a fully reconfigurable miniaturized helical filter is presented and demonstrated using a second-order bandpass filter. It is shown that without the requirement of any moving parts, this filter can reconfigure to have Butterworth-response behavior to Chebyshev-response behavior instantaneously. The reconfigurable filter achieves absolute constant bandwidth and is demonstrated by showing measured results of 8 MHz throughout the sweep as well as 10 MHz. Additionally, measurements that prove the reconfigurable filter can achieve constant fractional bandwidth of 5% are also demonstrated. The total tuning range is measured to be 140-180 MHz while having an insertion loss of 2.35-3.11 dB.

This concept allows for specific biasing values to be stored and put in action based upon a given conditions or requirements. Thereby, this device is a strong candidate for modern integrated systems.

## Chapter 5

### Fully 3D-Printed Helical Resonators

#### 5.1 Introduction

3D-printing technologies have enabled an inexpensive method of rapidly prototyping microwave components [22]–[24]. It is becoming an increasingly attractive alternative method of fabrication as manufactures are producing 3D-printers with very high resolution. It was demonstrated in Chapter 2-4 that 3D-printing technologies have enabled a quick and easy way to prototype a helical resonator by simply 3D-printing the cavity. This not only bypasses the expense of a block of copper but also the expense of having the copper manufactured by a professional. A typical method of realizing helical resonator filters often involves robust manufacturing such CNC machining, which can not only be expensive but time consuming. Furthermore, for an accurate fabrication and to compensate for inaccuracies presented during the manufacturing process, tuning screws are utilized to optimize the filter’s performance. Recently, a method of 3D-printing a fourth-order bandpass helical filter is introduced in [21]. In this publication, the filter is designed to operate at a fixed frequency and no size reduction is implemented to the design. In this chapter, the design guidelines demonstrated in Chapter 2 will be utilized to fabricate

a fully 3D-printed helical resonator [30]. A comparison will also be made between the characterized helical resonator in Chapter 2 and the one presented in this chapter. While the focus is on the 3D-fabrication, the comparison is to evaluate and test current 3D-printing capabilities.

## 5.2 Design

First, a quick summary of the guidelines presented in Chapter 2 are as follows. The preliminary conditions of the helical resonator includes an operating frequency at approximately the middle of the VHF band, such as 200 MHz, and a relatively high unloaded  $Q$  of 1000. From these basic specification, the cavity size, the helix diameter, and the number of turns can be obtained from (5.1) and (5.2), as they are all functions of the resonant frequency and the unloaded  $Q$  [26].

$$D = \frac{0.508 Q_{un}}{\sqrt{f_o}} \quad (5.1)$$

$$N = \frac{48.26 \times 10^6}{f_0 D} \quad (5.2)$$

where  $D$  is the diameter of the inner cavity and  $N$  is the number of turns in the helix. Expressions (5.1) and (5.2) have been modified to include SI units. As a result, a resonator with 6.7 turns and a cavity diameter of approximately 36 mm, yields an internal volume of approximately 38 cm<sup>3</sup>. Although the resonator is significantly smaller than a coaxial resonator, it is still considerably large. The component contributing the most to the cavity size is the helix, which provides the inductive loading to the cavity. Heavy capacitive loading can be used to miniaturize the cavity, which offsets the inductance. Further

information on obtaining the rest of the design parameters is outlined in Chapter 2 and [26]. Considering all the design guidelines, the final helical resonator was designed and optimized using Ansys HFSS. A conceptual model of this resonator is shown in Fig. 5.1. The cross section view of the weakly-coupled helical resonator, with all dimensions labeled, is shown in Fig. 5.2. The main parameters for a  $Q$  of 300 with varactors modeled as ideal capacitors are listed in Table 5.1.

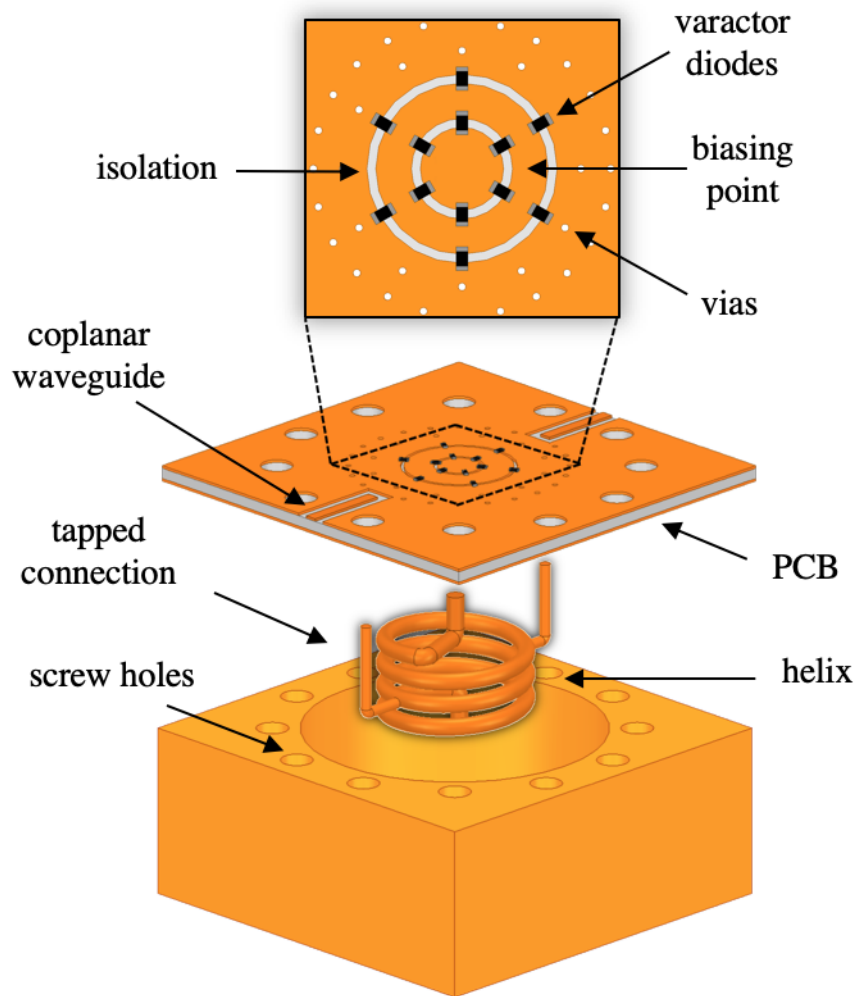


Figure 5.1: Exploded model of a highly miniaturized 3D-printed tunable helical resonator with varactor diodes mounted on the PCB.

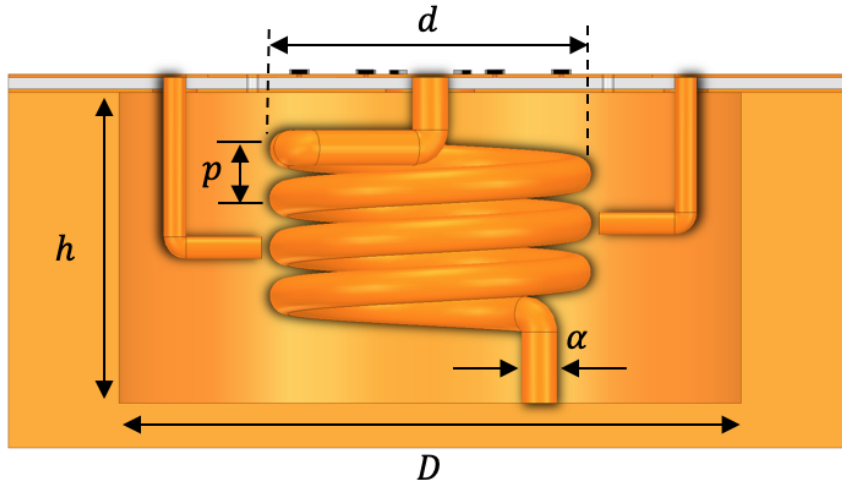


Figure 5.2: Internal view of the proposed 3D-printed helical resonator with defined parameters.

Table 5.1:  
3D-Printed Helical Resonator Design Parameters

Property	Value
Cavity diameter, $D$	28 mm
Helix diameter, $d$	14.4 mm
Cavity height, $h$	14 mm
Helix line diameter, $\alpha$	1.6 mm
Pitch, $p$	2.2 mm
Number of turns, $N$	3.4

### 5.2.1 Fabrication & Experimental Validation

As this work is focuses on a 3D-printed fabrication, there was a small issue that was found when trying to obtain a 3D-print file (.stl) file from HFSS. There doesn't seem to exist a simple or direct way to go from a HFSS design to a 3D-print file (e.g., .stl). In order to get around this issue, the file containing the model in HFSS needs to be exported from HFSS to SOLIDWORKS and then

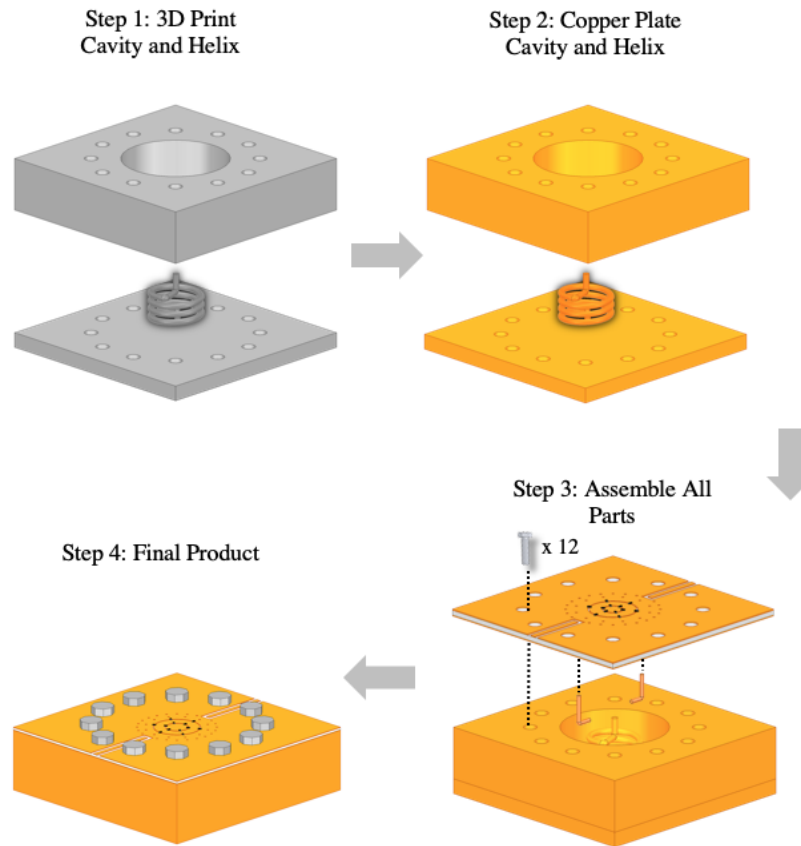


Figure 5.3: Illustration of the fabrication process. Starting from 3D-printing, then to copper plating, assembling the parts, and the final product.

to a 3D printer. This is accomplished by the following three step procedure. First, export the HFSS file as an “ACIS SAT Files (\*.sat)”, preferably an earlier version such as version 15. This part is important as the complex geometry of the helix is not supported by most file types. Next, import the file into SOLIDWORKS. From this point on, the file can be saved as a .stl file and is ready to 3D print. Once the 3D-printing process is complete, the structures are put through a metallization process (further information is on the metallization process is found in Chapter 5).

The geometry of the internal parameters of the 3D-printed helical resonator

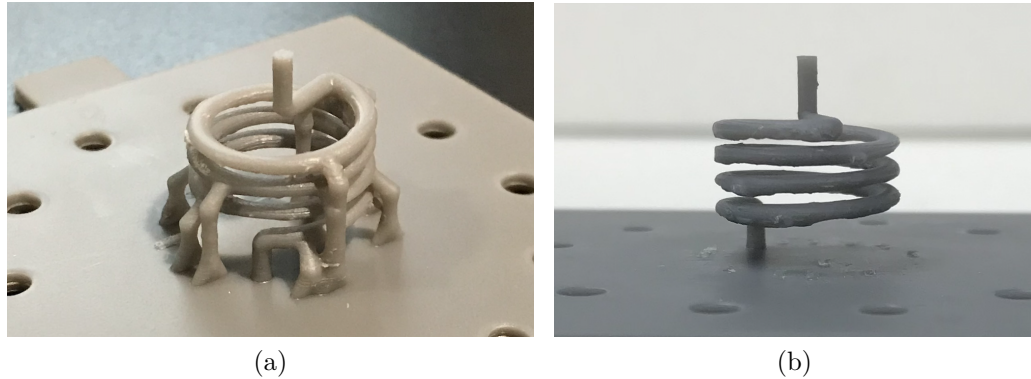


Figure 5.4: (a) Photograph of the 3D-printed helix with printed supports and a (b) photograph after the removal of supports.

is illustrated in Fig. 5.2. An overview of the process of realizing this resonator is shown in Fig. 5.3. The cavity and helix were realized by first 3D-printing the structures and then put through a metallization process. As seen from Fig. 5.3, the cavity is now 3D-printed in two parts, the base and helix as one part, and the remaining cavity part as the other (as opposed to one solid cavity from Chapter 2). Supports are required during the 3D-printing process to ensure the helix is printed with the correct pitch as seen in Fig.5.4a. Fabricating the cavity in this manner allows for a simple removal of the supports when the 3D-printing process is finished as there is no obstruction at any point around the helix. Upon the removal of the supports, uneven areas may result where the supports attached to the helix and/or base. To smooth these areas, small sized files are used. A photograph of the base with the helix after the removal of supports and sanded down can be seen in Fig.5.4b. The 3D printer that was used to print the cavity, base, and the helix is a table-top commercially available 3D printer from Formlabs (Form 2) utilizing photopolymer resin (RS-F2-GPWH-04).

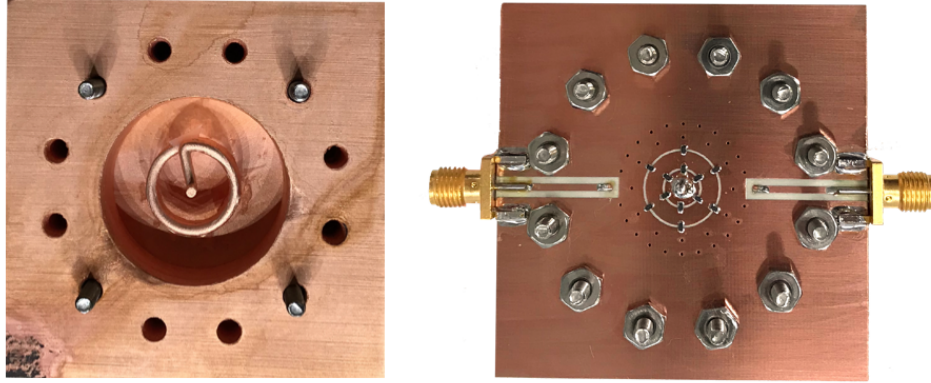


Figure 5.5: Photographs of the fabricated fully 3D-printed helical resonator. Cover removed to show helix (left) and fully assembled (right).

In preparation for metallization, the 3D-printed structures were submerged in an ultrasonic bath of isopropyl alcohol in order to treat the surfaces. Metallization is then carried out in three steps. In the first step, a seed layer consisting of palladium is chemically deposited on the 3D-printed surface. The seed layer provides a thin layer on the nonmetallic material, which acts like an adhesive layer for the sequent metallization. Then, the 3D-printed structure is electroless-copper-plated. This step is a very crucial step in the whole fabrication procedure as it forms a very thin layer of conducting surface all over the structure. Finally, the structure is electroplated with a thick layer of copper. The cavity lid was achieved by processing a 0.508 mm-thick microwave laminate (RO4350B from Rogers Corporation). The PCB process begins with drilling using a benchtop milling machine from LPKF in order to achieve the holes for the bolts, fiducials, and vias. Fiducials are simply holes that are drilled near the corners of the PCB, which allows the milling machine to read and base future processes according to the reference of the fiducials if the board is removed in between processes. Once all the holes have been drilled, metallization is then performed on the PCB to insure an electri-



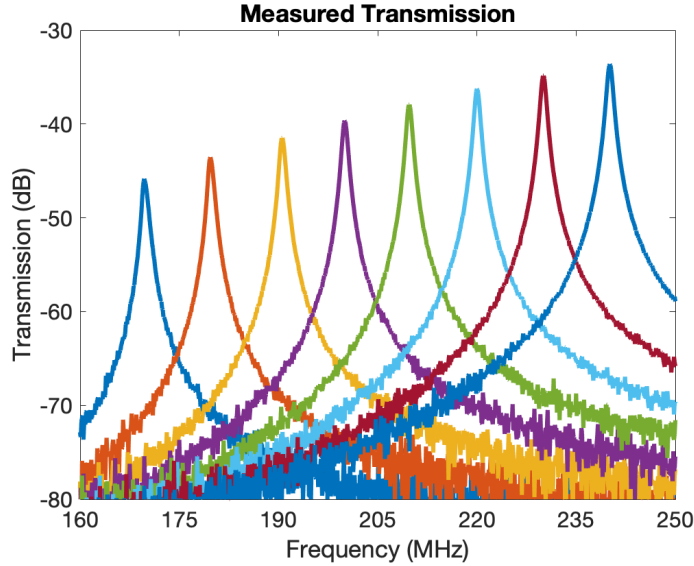


Figure 5.6: Measured frequency response of the fully 3D-printed resonator.

cal connection between the top and bottom layer of copper. Then, the PCB is put through a photolithography process in order to achieve the coplanar waveguide transmission lines. The variable capacitive loading is achieved by utilizing varactor diodes SMV1405-040LF by Skyworks Solutions. By applying a 0-30 V reverse biasing to the isolated copper ring shown in Fig. 5.1, a variable capacitance of 0.56-2.82 pF is obtained. A solid-core 18 gauge copper wire was used to achieve the L-bar wire, which was used to couple into the helix from the coplanar waveguides as shown in Fig. 5.2. As this resonator is intended to be weakly coupled in order to extract electrical performances, a gap was intentionally imposed between the end of the L-bar wire and the helix. The L-bar wire is soldered to the PBC where it makes an electrical connection with the coplanar waveguides and placed adjacent to the helix. A photograph of the fabricated 3D-printed helical resonator is shown in Fig. 5.5.

Based on Fig. 5.6, the tunable frequency range is from 170-240 MHz which is comparable to the tunable range of 150-230 MHz that was presented in

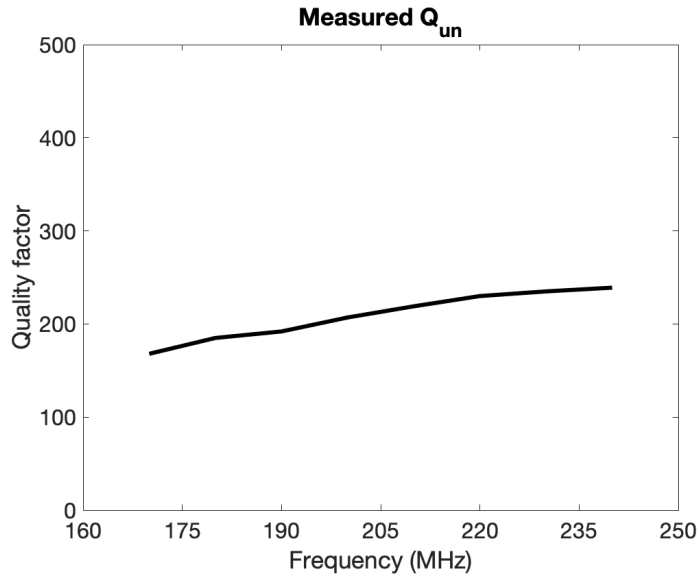


Figure 5.7: Measured unloaded  $Q$  from the 3D-printed helical resonator.

Chapter 1. Fig. 5.7 shows the unloaded  $Q$  of the proposed helical resonator. It can be seen that the unloaded  $Q$  ranges from 185-239, which again is comparable to the results presented in Chapter 1.

### 5.3 Discussion on Capabilities & Improvements

The tuning range of the fully 3D-printed resonator is slightly shorter than the helical resonator in Chapter 2. One possibility is that a varactor diode was not soldered on correctly therefore reducing the total tuning range. Another observation is that the unloaded  $Q$  of the 3D-printed resonator is reduced at lower frequencies ( $< 200$  MHz), when compared to the resonator in Chapter 2. This can be attributed to the 3D-printed structure not receiving enough copper during the copper plating process. This results in a copper thickness less than one skin depth, which is not thick enough for the tuning range that reached below 200 MHz.

Another contributor could be that the diameter was not consistent along the helix due to the removal of the supports as seen in Fig. 5.4b. Also, during the metallization process, the 3D-printed structures were submerged in heated plating tanks, which caused the helix to shrink. This uncontrollable effect caused inaccuracies in the pitch  $p$ . Nevertheless, Table 5.2 shows good agreement between the proposed resonator and the one presented Chapter 2.

Table 5.2:  
 $Q_{un}$  Comparison of the 3D-Printed and Wire-Formed Helix

Resonant frequency $f_o$ (MHz)	180	190	200	210	220
3D-printed helix $Q_{un}$	185	192	207	219	235
Wire-formed helix $Q_{un}$	208	211	214	223	234

## 5.4 Conclusion

A 3D-printed highly miniaturized, tunable helical resonator is presented for the first time. PCBs are employed to achieve the cavity lid, which fastened the varactors. PCBs also provide a place to host future integration of RF components directly on the top copper layer. A miniaturized tunable helical resonator is 3D-printed and characterized. A measured continuous tuning frequency of 170-240 MHz with an unloaded  $Q$  of 168-239 is measured. The 3D-printed resonator is also compared to the performance of a fabricated helical resonator employing a wire-formed helix that is presented in Chapter 1, showing comparable results. Based on the results shown in this chapter, 3D-printing technologies are sufficient for rapidly prototyping complex structures in a lab environment.

## Chapter 6

### Conclusion

The overcrowded RF spectrum demands development of frequency-agile technology in the sub-gigahertz frequency range. This thesis presented a method of combining high performance resonator structures with rapid tuning semiconductor technology for modern integrated systems. Therefore, a highly miniaturized VHF helical resonator utilizing varactor diodes for frequency tuning is demonstrated for the first time. This integrated technology allows for  $Q$  values in the 200s while having rapid continuous tuning through the frequency range without mechanical change. Furthermore, PCBs are used to combine helical-resonator technology with planar platforms for the first time. Novel feeding mechanisms are realized using coplanar waveguides and L-bars that provide external coupling to the helical filter, eliminating the traditional method of connectorizing helical resonators/filters. Additionally, this configuration resulted in two TZs, one on the upper and lower side of the passband of an inline second-order helical filter. This characteristic is something that is not commonly seen among coupled resonators.

All these techniques lead to a fully reconfigurable filter having full control over the center frequency, inter-resonator coupling, and external coupling. It is shown that by having control over these parameters, the reconfigurable filter

achieves either constant absolute bandwidth, constant fractional bandwidth, or constant insertion loss level throughout the frequency-tuning range. It has also been shown that all the tuning capabilities reported in this work were achieved by electronically tuning the filter; therefore, no mechanical or physical changes were made while tuning any of the devices reported.

3D-printing printing technologies are shown to be a great method of fabricating prototypes for VHF helical resonator/filters. A comparison was made between two identical helical resonators with the exception of the helix. One resonator utilized a wire-formed helix while the other was a 3D printed helix. The results are in very good agreement and demonstrated that 3D-printing technologies can be used to prototype complex microwave components in a laboratory environment, such as a helical structures.

In conclusion, this work presented a method of efficiently using sections of the spectrum in the VHF band. The proposed fully reconfigurable filter has the advantage of a highly miniaturized profile, state-of-the-art tuning components and integration, and flexible tuning capabilities, making this device a strong candidate for future sophisticated RF systems.

## 6.1 Future Direction

A look-up table can be made to store capacitive values corresponding to the specific voltage biasing being applied to the varactors. This enables a microcontroller to have on-demand instantaneous reconfigurability. Another feature that could be investigated in future work is the location of the TZs. It is shown what causes the TZs and can be replicated with a simple schematic performed in AWR. Having the ability to steer the TZs closer or further away from the passband increases the filter's tuning flexibility. This has the potential to re-

duce size, weight, and cost of the device by eliminating additional resonators that are conventionally required to add cross-coupling.

A linearity test was not performed, however it is well known that the power handling is going to be limited by the varactor diodes. One way to improve the proposed reconfigurable filter is to achieve better power handling. Typical applications found in the VHF-UHF range include satellite and ground-based communication systems. These types of applications require devices with high power handling.

## References

- [1] S. J. Shellhammer, A. K. Sadek, and W. Zhang, “Technical Challenges for Cognitive Radio in the TV White Space Spectrum”, in *2009 Information Theory and Applications Workshop*, 2009, pp. 323–333. DOI: 10.1109/ITA.2009.5044964.
- [2] U. S. D. of Commerce, *United States Frequency Allocations Chart 2016 - the Radio Spectrum*, (Accessed: 29 Apr. 2019).
- [3] J.-S. Hong, *Microstrip Filters for RF/Microwave Applications*. Hoboken, NJ, USA: Wiley, 2011.
- [4] P. Vizmuller, “Filter with Helical and Helical Folded Resonators”, Jan. 1987.
- [5] T. Lee, S. Cheon, and J. Park, “Ultracompact UHF Tunable Filter Embedded Into Multilayered Organic Packaging Substrate”, *IEEE Transactions on Components, Packaging and Manufacturing Technology*, vol. 2, no. 1, pp. 46–52, 2012, ISSN: 2156-3950. DOI: 10.1109/TCPMT.2011.2167620.
- [6] F. A. Houndonougbo, R. Costes, J. Fan, A. Crunteanu, V. Madrangeas, D. Cros, M. Pate, J. P. Ganne, and P. Monteil, “A 380 – 420 MHz Two-Pole Tunable Filter Using New Ferroelectric Composite Capacitors”, in *The 40th European Microwave Conference*, 2010, pp. 1134–1137. DOI: 10.23919/EUMC.2010.5616223.
- [7] and W. D. Yan and E. P. W. Horne, “Broadband Tunable Filters Using High Q Passive Tunable ICs”, in *2008 IEEE MTT-S International Microwave Symposium Digest*, 2008, pp. 951–954. DOI: 10.1109/MWSYM.2008.4632991.
- [8] H. Jiang, B. Lacroix, K. Choi, Y. Wang, A. T. Hunt, and J. Papapolymerou, “A Compact Ferroelectric Tunable Bandpass Filter with Flexible

- Frequency Responses”, in *2012 IEEE International Conference on Wireless Information Technology and Systems (ICWITS)*, 2012, pp. 1–4. DOI: 10.1109/ICWITS.2012.6417702.
- [9] K. Entesari, K. Obeidat, A. R. Brown, and G. M. Rebeiz, “A 25–75-MHz RF MEMS Tunable Filter”, *IEEE Transactions on Microwave Theory and Techniques*, vol. 55, no. 11, pp. 2399–2405, 2007, ISSN: 0018-9480. DOI: 10.1109/TMTT.2007.908674.
- [10] R. D. Streeter, C. A. Hall, R. Wood, and R. Mahadevan, “VHF High-Power Tunable RF Bandpass Filter Using Microelectromechanical (MEM) Microrelays”, *International Journal of RF and Microwave Computer-Aided Engineering*, vol. 11, no. 5, pp. 261–275, 2001. DOI: 10.1002/mmce.1035.
- [11] Y. Shim, Z. Wu, and M. Rais-Zadeh, “A High-Performance Continuously Tunable MEMS Bandpass Filter at 1 GHz”, *IEEE Transactions on Microwave Theory and Techniques*, vol. 60, no. 8, pp. 2439–2447, 2012, ISSN: 0018-9480.
- [12] S. Bantas and Y. Koutsoyannopoulos, “CMOS Active-LC Bandpass Filters with Coupled-Inductor Q-Enhancement and Center Frequency Tuning, year=2004, volume=51, number=2, pages=69-76, doi=10.1109/TCSII.2003.821521, issn=1549-7747, month=Feb,” *IEEE Transactions on Circuits and Systems II: Express Briefs*,
- [13] E. E. Hoppenjans and W. J. Chappell, “The Use of High Q Toroid Inductors for LTCC Integrated Tunable VHF Filters”, in *2009 IEEE MTT-S International Microwave Symposium Digest*, 2009, pp. 905–908. DOI: 10.1109/MWSYM.2009.5165844.
- [14] R. R. Mansour, “High-Q Tunable Dielectric Resonator Filters”, *IEEE Microwave Magazine*, vol. 10, no. 6, pp. 84–98, 2009, ISSN: 1527-3342. DOI: 10.1109/MMM.2009.933591.
- [15] W. W. Macalpine and R. O. Schildknecht, “Coaxial Resonators with Helical Inner Conductor”, *Proceedings of the IRE*, vol. 47, no. 12, pp. 2099–2105, 1959, ISSN: 0096-8390. DOI: 10.1109/JRPROC.1959.287128.
- [16] E. Doumanis, G. Goussetis, and S. A. Kosmopoulos, “Inline Interdigital Pseudo-Elliptic Helical Resonator Filters”, *IEEE Microwave and Wire-*



- less Components Letters*, vol. 21, no. 8, pp. 400–402, 2011, ISSN: 1531-1309. DOI: 10.1109/LMWC.2011.2160162.
- [17] W. Sichak, “Coaxial Line with Helical Inner Conductor”, *Proceedings of the IRE*, vol. 42, no. 8, pp. 1315–1319, 1954, ISSN: 0096-8390. DOI: 10.1109/JRPROC.1954.274829.
- [18] and, “High Performance Helical Resonator Filters”, in *34th European Microwave Conference, 2004.*, vol. 2, 2004, pp. 989–992.
- [19] K. Puglia, *Code Domain Analysis on W-CDMA User Equipment Transmitters*, (Accessed: 29 Apr. 2019).
- [20] D. Psychogiou and D. Peroulis, “Tunable VHF Miniaturized Helical Filters”, *IEEE Transactions on Microwave Theory and Techniques*, vol. 62, no. 2, pp. 282–289, 2014.
- [21] X. Shang, J. Li, C. Guo, M. J. Lancaster, and J. Xu, “3-D Printed Filter Based on Helical Resonators with Variable Width”, in *2017 IEEE MTT-S International Microwave Symposium (IMS)*, 2017, pp. 1587–1590. DOI: 10.1109/MWSYM.2017.8058936.
- [22] P. A. Booth and E. Valles Lluch, “Realising Advanced Waveguide Bandpass Filters Using Additive Manufacturing”, *IET Microwaves, Antennas Propagation*, vol. 11, no. 14, pp. 1943–1948, 2017, ISSN: 1751-8725. DOI: 10.1049/iet-map.2017.0170.
- [23] H. Saeidi-Manesh, S. Saeedi, M. Mirmozafari, G. Zhang, and H. H. Sigmarsson, “Design and Fabrication of Orthogonal-Mode Transducer Using 3-D Printing Technology”, *IEEE Antennas and Wireless Propagation Letters*, vol. 17, no. 11, pp. 2013–2016, 2018, ISSN: 1536-1225. DOI: 10.1109/LAWP.2018.2847654.
- [24] M. Mirmozafari, S. Saeedi, H. Saeidi-Manesh, G. Zhang, and H. H. Sigmarsson, “Direct 3-D Printing of Nonplanar Linear-Dipole-Phased Array Antennas”, *IEEE Antennas and Wireless Propagation Letters*, vol. 17, no. 11, pp. 2137–2140, 2018, ISSN: 1536-1225. DOI: 10.1109/LAWP.2018.2860463.
- [25] Z.-Y Zhao, P.-H Li, K.-L Cheng, W.-Q Coa, and K.-H Chen, “High Power VHF Frequency-Hopping Filtes with High Suppression of Second

- Harmonic”, *Progress in Electromagnetics Research Letters*, vol. 20, Jan. 2011.
- [26] A. I. Zverev, *Handbook of Filter Synthesis*. New York, NY, USA: Wiley, 1967.
- [27] E. Arroyo-Diaz, S. Saeedi, and H. Sigmarsson, “Frequency-Agile Coplanar-Waveguide-Fed Miniaturized Helical Resonator Filters”, in *2019 IEEE 20th Wireless and Microwave Technology Conference (WAMICON)*, Cocoa Beach, Florida, USA, Apr. 2019.
- [28] G. L. Matthaei, L. Young, and E. M. T. Jones, *Microwave Filters, Impedance Matching Networks, and Coupling Structures*. Norwood, MA, USA: Artech House, 1980.
- [29] S. Saeedi, J. Lee, and H. Sigmarsson, “A New Property of Maximally-Flat Lowpass Filter Prototype Coefficients with Application in Dissipative Calculations”, *Progress in Electromagnetics Research C*, vol. 63, Mar. 2016.
- [30] E. Arroyo-Diaz, S. Saeedi, and H. Sigmarsson, “3D-Printed Tunable Helical Resonators for Miniaturized VHF Filters”, in *2019 IEEE Texas Symposium on Wireless and Microwave Circuits and Systems (WMCS)*, Waco, Texas, USA, Mar. 2019.